T.R.
BOLU ABANT İZZET BAYSAL UNIVERSITY
INSTITUTE OF GRADUATE STUDIES
Department of Physics

USING MACHINE LEARNING METHOD TO SEARCH THE ANOMALOUS QUARTIC GAUGE COUPLINGS VIA TRI-PHOTON PRODUCTION AT FUTURE HADRON COLLIDERS

MASTER OF SCIENCE

CEREN HELVECİ

ACADEMIC SUPERVISOR
Prof. Dr. Abdulkadir ŞENOL

BOLU, ARALIK - 2023

APPROVAL OF THE THESIS

USING MACHINE LEARNING METHOD TO SEARCH THE ANOMALOUS QUARTIC GAUGE COUPLINGS VIA TRI-PHOTON PRODUCTION AT FUTURE HADRON COLLIDERS submitted by Ceren HELVECİ and defended before the Examining Committe Members listed below in partial fulfillment of the requirements for the degree of **Master of Science** in **Department of Physics, Institute of Graduate Studies of Bolu Abant Izzet Baysal University in 22.12.2023** by

Examining Committee Members	**Signature**
Supervisor Prof. Dr. Abdulkadir ŞENOL Bolu Abant Izzet Baysal University	....
Member Prof. Dr. Haluk DENİZLİ Bolu Abant Izzet Baysal University	....
Member Prof. Dr. İlkay TÜRK ÇAKIR Ankara University	....

Prof. Dr. İbrahim KÜRTÜL

Director of Instıtute of Graduate Studies

ETHICAL DECLARATION

In this thesis dissertation that was properly prepared according to the Thesis Writing Rules of Bolu Abant Izzet Baysal University of the Institute of Graduates Studies, I hereby declare that;

- All data, information, and documents presented in the thesis were obtained in accordance with the academic and ethical rules,
- All data, documents, assessments, and results were presented in accordance with the scientific ethical and moral rules,
- All works that were benefitted in the thesis were appropriately cited,
- No alteration was made in the data used,
- Study presented in this thesis is original,

Otherwise, I declare that I accept the loss of all my rights in case any contradiction that may arise against me.

The similarity rate obtained by using the Turnitin program, a plagiarism detection software, is within the limits approved by the University Senate.

____

Ceren HELVECİ

ABSTRACT

USING MACHINE LEARNING METHOD TO SEARCH THE ANOMALOUS QUARTIC GAUGE COUPLINGS VIA TRI-PHOTON PRODUCTION AT FUTURE HADRON COLLIDERS

MSC THESIS
CEREN HELVECİ
BOLU ABANT IZZET BAYSAL UNIVERSITY
INSTITUTE OF GRADUATE STUDIES
DEPARTMENT OF PHYSICS
(SUPERVISOR: PROF. DR., ABDULKADİR ŞENOL)
BOLU, DECEMBER 2023
xii + 54 pages

Examining the self-couplings of gauge bosons, as dictated by the non-Abelian gauge symmetry in the Standard Model (SM), provides invaluable insights into the SM's gauge structure. Any departure from SM's predictions regarding gauge boson self-coupling could hint at the presence of new physics beyond the SM. This involves adjusting self-interactions through an effective field theory approach. This study aims to investigate anomalous quartic gauge dimension-8 couplings related to γγγγ and γγγZ vertices via tri-photon production in future hadron colliders, namely the HL-LHC ($\sqrt{s}$=14 TeV) and the FCC-hh ($\sqrt{s}$=100 TeV) with integrated luminosities of 3 ab^{-1} and 30 ab^{-1}. Generated events, considering parton showering and detector effects, are analyzed using Monte Carlo methods and also using machine learning methods which are called TMVA with Boosted Decision Trees. Limits of anomalous quartic gauge couplings $f_{T8}/\ \Lambda^4$ and $f_{T9}/\ \Lambda^4$, obtained at a 95% confidence level, with and without systematic errors for both future hadron colliders. Results for the FCC-hh collider indicate that constraints on anomalous quartic gauge couplings are about three orders of magnitude stronger than the best experimental limits by the ATLAS collaboration at the LHC. Factoring in a realistic 10% systematic uncertainty, the limits degrade by about one order of magnitude but still surpass those reported by ATLAS by two orders of magnitude.

KEYWORDS: Tri-photon production, Anomalous Quartic Gauge Couplings Dimension-8 operators, TMVA, Effective Field Theory

ÖZET

GELECEKTEKİ HADRON ÇARPIŞTIRICILARINDA MAKİNE ÖĞRENMESİ TEKNİĞİ KULLANILARAK ANORMAL DÖRTLÜ AYAR BAĞLAŞIMLARININ ÜÇ-FOTON ÜRETİMİYLE ARAŞTIRILMASI
YÜKSEK LİSANS TEZİ
CEREN HELVECİ
BOLU ABANT İZZET BAYSAL ÜNİVERSİTESİ
LİSANSÜSTÜ EĞİTİM ENSTİTÜSÜ
FİZİK ANABİLİM DALI
(TEZ DANIŞMANI: PROF. DR., ABDULKADİR ŞENOL)
BOLU, ARALIK - 2023
xii + 54 sayfa

Standart Model'deki Abelyen olmayan ayar simetrisinin gerektirdiği şekilde ayar bozonlarının kendi kendine eşleşmelerinin incelenmesi, SM'nin ayar yapısına dair çok değerli bilgiler sağlar. SM'nin ayar bozonu kendi kendine eşleşmesine ilişkin tahminlerinden herhangi bir sapma, SM'nin ötesinde yeni fiziğin varlığına işaret edebilir. Bu, etkili bir alan teorisi yaklaşımı kullanarak kendi kendine etkileşimleri ayarlamayı içerir. Bu çalışmanın amacı, gelecekteki hadron çarpıştırıcıları olan HL-LHC (14 TeV) ve FCC-hh (100 TeV) üzerinde, entegre luminositeleri sırasıyla 3 ve 30 olan HL-LHC ve FCC-hh'de, $\gamma\gamma\gamma\gamma$ ve $\gamma\gamma\gamma Z$ vertex'leri ile ilişkilendirilen anormal dördüncül kalibre boyut-8 bağlantıları tri-foton üretimi aracılığıyla incelemektir. Üretilen olaylar, parton duşu ve dedektör etkileri göz önüne alınarak Monte Carlo yöntemleri kullanılarak analiz edilmiş ve aynı zamanda Boosted Decision Trees adı verilen TMVA ile makine öğrenimi yöntemleriyle de incelenmiştir. f_{T8}/Λ^4 ve f_{T9}/Λ^4 anormal dörtlü ayar bağlantılarının limitleri, gelecekteki her iki hadron çarpıştırıcısı için sistematik hatalarla ve sistematik hatalar olmadan %95 güven düzeyinde elde edildi. FCC-hh'nin sonuçları, anormal dördüncü derece ayar bağlantıları üzerindeki kısıtlamaların, LHC'deki ATLAS işbirliğinin en iyi deneysel limitlerinden yaklaşık üç kat daha güçlü olduğunu göstermektedir. Gerçekçi %10'luk sistematik belirsizlik hesaba katıldığında, sınırlar yaklaşık bir kat azalıyor ancak yine de ATLAS tarafından rapor edilen değerleri iki kat aşıyor.

ANAHTAR KELİMELER: Üç-foton Üretimi, Anormal Dörtlü Ayar Kuplajları, Boyut-8 Operatörleri, TMVA, Efektif Alan Teorisi

TABLE OF CONTENTS

LIST OF FIGURES

Page

LIST OF TABLES

Page

LIST OF ABBREVIATIONS AND SYMBOLS

SM	: Standard Model
BSM	: Beyond the Standard Model
LHC	: Large Hadron Collider
HL-LHC	: High-Luminosity Large Hadron Collider
FCC-hh	: Future Circular Hadron-Hadron Collider
CERN	: Conseil Européen pour la Recherche Nucléaire
aQGC	: Anomalous Quartic Gauge Coupling
BSM	: Beyond the Standard Model
TMVA	: Toolkit for Multivariate Analysis
BDT	: Boosted Decision Tree
EW	: Electro-weak
EFT	: Effective Field Theory
UV	: Unitarity Violation
VBS	: Vector Boson Scattering

ACKNOWLEDGEMENTS

First and foremost, I would like to express my infinite gratitude to my thesis advisor, Prof. Dr. Abdulkadir Şenol. His valuable guidance, patience, and experience played a significant role in the realization of this study.

I would also like to extend my thanks to Prof. Dr. Haluk Denizli, with whom I had the opportunity to work collaboratively. His wealth of knowledge and guidance contributed to enhancing the quality of this thesis.

I want to convey my deep appreciation to my family, especially my mother, Hatice Helveci. Her consistently uplifting support and understanding empowered me throughout this challenging process.

Special thanks are also due to my brother, Uğur Helveci, and his wife, Ezgi Helveci. Their encouragement and support were invaluable, and I am grateful for their presence in my life.

1. INTRODUCTION

The Standard Model (SM) stands as a cornerstone in high-energy physics, offering a detailed framework to explain the behaviors and interactions of elementary particles in the sub-atomic world. Its precision is evident in accurately portraying electromagnetic, strong, and weak interactions, substantiated by rigorous experimental confirmations. However, despite its widespread acceptance, the SM encounters limitations when extended to encompass gravity, particularly in the context of grand unified forces or a quantum theory of gravity. A pivotal moment in the validation of the SM occurred with the identification of the Higgs boson, marking the culmination of the particle spectrum within this theoretical framework. The Higgs mechanism (1,2), introduced by Peter Higgs and collaborators in the 1960s, elucidated the means by which particles acquire mass within the SM paradigm.

The groundbreaking discovery of the Higgs boson (1,2) by the Large Hadron Collider (LHC) in 2012 served as the final piece in confirming the existence of all predicted particles within the SM. While the SM stands as a robust framework, its inherent limitations propel the scientific community towards the pursuit of New Physics (NP) beyond its confines. To date, experimental endeavors at higher energy levels have yet to yield conclusive evidence of NP. Nevertheless, the ongoing and forthcoming efforts at cutting-edge high-energy particle colliders, including the LHC and the Future Circular Hadron Collider (FCC-hh) at CERN, offer promising avenues to explore and potentially detect Beyond the Standard Model (BSM) physics. The integration of innovative technologies and the attainment of high luminosity in these colliders not only offer unprecedented opportunities but also significantly enhance the prospects of unraveling new facets of particle physics and expanding our understanding of the fundamental constituents of the universe.

The dimension-8 effective operators associated with anomalous quartic $\gamma\gamma\gamma\gamma$ and $\gamma\gamma\gamma Z$ vertices have been examined within the context of the tri-photon process at the future hadron colliders. This investigation includes realistic detector effects in both the signal and all relevant background process productions. Leveraging the Toolkit for Multivariate Data Analysis (TMVA), and its integration of boosted decision trees (BDTs), a prominent machine learning method rapidly evolving in particle physics, enhances the discernment between the signal and pertinent backgrounds. Following the derivation of sensitivities regarding aQGC, a comparative analysis is conducted with existing experimental constraints, accompanied by insightful commentary on the numerical findings.

The outline of the thesis consists of a comprehensive exploration, beginning with an in-depth discussion of the theoretical framework that encompasses the SM of particles and BSM in Chapter 1. This chapter particularly emphasizes the Effective Field Theory (EFT) approach, laying a solid foundation for a nuanced understanding. Chapter 2 provides a concise review of the LHC, HL-LHC, and FCC-hh detectors. Chapter 3 outlines the specific aims and scope of the study, setting the stage for the subsequent detailed discussions. Chapter 4 delves into the intricacies of generating both signal and background processes, detailing the generation of simulated data using TMVA methods. This chapter also encompasses the measurement of aQGC and the optimization of event selection, crucial steps in ensuring the robustness of the analysis.

1.1 Standard Model of Elementary Particles

The field of particle physics emerged in the early 1900s, a time of great scientific progress and paradigm shifts. The discovery and evolution of quantum mechanics, a groundbreaking theory that revolutionized our understanding of the subatomic world, was at the heart of this transformative period. Scientists during this era faced a number of perplexing phenomena that classical physics could not fully explain. The photoelectric effect, the behavior of atoms, and the properties of radiation produced by specific elements all contradict existing Newtonian principles. As a result, eminent physicists such as Max Planck, Albert Einstein, Niels Bohr, and Werner Heisenberg initiated the development of quantum mechanics. In 1900, Max Planck introduced the concept of quantized energy levels, which suggests that energy is released or absorbed in specific packets known as quanta. Later in 1905, Einstein's explanation of the photoelectric effect introduced the idea of light behaving as both particles (photons) and waves, further strengthening the theory of quantum mechanics. In 1913, Niels Bohr developed the Bohr model, which helped explain how electrons behave in atoms, based on the idea of quantized electron energy levels. It successfully explained hydrogen's emission and absorption spectra, supporting the wave-particle duality of quantum mechanics. However, it was Werner Heisenberg's formulation of matrix mechanics in 1925 and Erwin Schrödinger's development of wave mechanics in the same year that unified and extended these early quantum theories, giving rise to a new quantum formalism that described particles as both waves and particles, depending on the experimental context. With the establishment of quantum mechanics, scientists were on the brink of a revolution in understanding the fundamental building blocks of the universe.

In the following decades, particle accelerators and cosmic ray detectors became crucial tools for experimental physicists. The discovery of subatomic particles such as the electron, proton, and neutron unveiled a rich subatomic landscape, leading to the development of the first classification schemes for elementary particles. As experimental techniques progressed, physicists discovered numerous new particles with distinct properties and interactions. The notion of "strangeness," which Murray Gell-Mann and Kazuhiko Nishijima introduced in 1953, was instrumental in understanding the patterns and symmetries within these particles.

The Standard Model, as we know it today, began to take shape in the 1960s and 1970s. The development of quantum field theories, particularly quantum chromodynamics (QCD) and electroweak theory, allowed for the unification of electromagnetic and weak interactions. Sheldon Glashow, Abdus Salam, and Steven Weinberg (3,4,5) independently formulated the electroweak theory, explaining the unity between electromagnetism and the weak nuclear force.

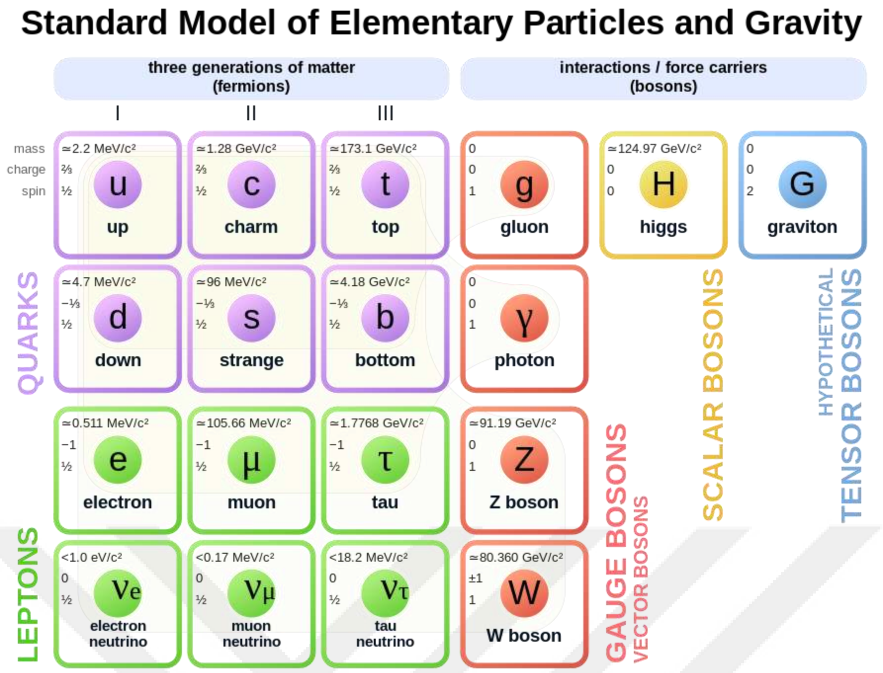

Figure 1.1. Standard Model of particles (6).

Figure 1.1 shows the elementary particles of SM. The SM classifies elementary particles into two groups depending on their spin: fermions and bosons. Fermions, one of the fundamental components in forming matter, have half-integer spin values and are divided into two fundamental subcategories called leptons and quarks.

Leptons have two groups including electron-like and neutrinos. Electron-like leptons with negative electric charges (e^-), while neutrinos (ν^l) are electrically neutral. Leptons are particles represented by a family of three generations. The generations of leptons are related to their masses and are not directly linked to their electric charges. There are six leptons, and each lepton has an associated neutrino, and each anti-lepton has an associated anti-neutrino with opposite charge. In the first generation of leptons, there is an electron and an electron neutrino, with the electron having a charge of -1, while the electron neutrino is neutral. Second generation leptons include muon and muon neutrino, and third generation leptons include tau and tau neutrino.

Quarks carry a specific charge called color charge also referred to as flavors and interact with the strong force. Like leptons, they are divided into three generations and there are six different types of quarks. These are up (u), down (d), strange (s), charm (c), top (t), and bottom (b) quarks. Each quark type has its own unique characteristics and charges. The electric charges of quarks are positive ⅔ for u, c, and t quarks, and negative ⅓ for d, s, and b quarks. The combination of quarks results in the formation of particles such as protons, neutrons, and other hadrons. First generations quarks bounding with protons (7).

Bosons have an integer spin value and are known as mediators of interaction between particles. Most of the bosons in the SM are used to ensure local gauge symmetry and are referred to as gauge bosons. Gauge bosons have a spin of one and are known as force carriers. These include the massless photon (γ) and gluons (g), as well as the massive W^-, W^+, and Z^0 bosons. Bosons which have mass and spin values, are also referred to as vector bosons. This designation arises from the fact that the spin operator has three eigenstates, and as a result, bosons possess three degrees of freedom, much like a vector in three-dimensional space. For massless bosons, only spins parallel or antiparallel to the direction of motion are allowed. The Higgs boson, on the other hand, is a different type. The Higgs boson is a scalar boson with a spin value of 0 and is considered as the source of mass. It is associated with the function of imparting mass to other particles.

In the sub-atomic world, our understanding of the fundamental forces that govern the behavior of the universe is encapsulated by four interactions: electromagnetic, strong nuclear, weak nuclear, and gravitational forces, each with its dedicated physical theory. While the SM successfully explains the electromagnetic, strong, and weak forces, it falls short in accounting for the gravitational force. The role of gauge bosons is pivotal in elucidating these interactions. In the case of electromagnetic force, particles carrying electric charge engage in the Exchange of photons, and these interactions are explained by Quantum Electrodynamics (QED) (8). The strong force, responsible for binding quarks within protons and neutrons, is transmitted through gluons. The dynamics of strong force interactions are explained by QCD. The weak force, responsible for processes like beta decay, is mediated by exchange particles called bosons. The W and Z bosons serve as force carriers associated with the weak interaction. The W bosons come in two types: W^+ carrying a positive electric charge, and W^- carrying a negative electric charge, while the Z^0 boson is electrically neutral. However, the weak force exhibits a much shorter range compared to electromagnetism, a characteristic attributed to the relatively large masses of the W and Z bosons (5). Lastly, gravity, described by general relativity, is a universal force that governs the dynamics of massive objects (9). Together, these four forces form the cornerstone of the Standard Model, providing a comprehensive framework for understanding the fundamental building blocks of the universe (10).

1.2 Beyond the Standard Model

Beyond the Standard Model (BSM) refers to theoretical physics frameworks that aim to extend the SM, which currently describes the fundamental particles and forces in the universe. The Standard Model has been remarkably successful in explaining particle interactions, but it leaves unanswered questions about phenomena like dark matter (11), dark energy (12), and neutrino masses. BSM theories propose new particles, forces, or symmetries to address these gaps. Examples include Grand Unified Theories (GUTs) (13), supersymmetry (SUSY) (14), and string theory (15). To provide a brief explanation of the aforementioned issues:

Dark energy: It is responsible for the observed accelerated expansion of the universe. Unlike ordinary matter and dark matter, dark energy doesn't clump together or interact with other forms of matter or radiation, making it challenging to detect or understand. The existence of dark energy was proposed to explain why galaxies move away from each other at an accelerating rate, contrary to what one might expect based on the gravitational attraction of matter. It remains one of the most significant puzzles in cosmology, and its exact nature is still a subject of active research. The term "dark energy" is used to describe this phenomenon, even though we don't yet know what this energy truly represents. Unlike gravity, which attracts objects together, dark energy has a repulsive effect, driving cosmic distances to grow larger. It's a fundamental component of the cosmos, comprising about 68% of the universe's total energy content.

Dark matter: Dark matter is a peculiar form of substance that does not emit, absorb, or interact with electromagnetic radiation, including light. This lack of interaction is the reason it is termed "dark," and its elusive nature prevents detection through conventional means. Constituting a substantial portion of the universe, dark matter accounts for 26% of the total energy in the cosmos and comprises over 80% of all matter. Its presence is deduced from gravitational effects on visible matter, galaxies, and galaxy clusters. The gravitational influence of dark matter plays a vital role in maintaining the cohesion of galaxies and shaping the large-scale structure of the cosmos.

Indeed, the gravitational force produced by dark matter is crucial for explaining the observed movements and clustering of galaxies. Despite its pivotal role in the structure and dynamics of the universe, the true identity of dark matter remains one of the most profound unsolved mysteries in contemporary astrophysics and particle physics. Ongoing experiments and observations aim to detect or gain a better understanding of this mysterious substance.

Neutrino masses: The Standard Model stands as a successful theory, providing an accurate description of the interactions among fundamental particles and fundamental forces. However, assuming zero masses for neutrinos contradicts many observations. Neutrinos interact through the weak nuclear force, and this interaction can lead to the phenomenon of neutrino oscillation, where different types of neutrinos can transform into each other (16,17). Neutrino oscillation serves as a crucial piece of evidence indicating that neutrinos must have non-zero masses.

Neutrino oscillation refers to the ability of one type of neutrino to transform into other types. This transformation is dependent on the neutrino mass. If neutrinos had zero masses, such transformations would not be possible. Hence, the observation of neutrino oscillation suggests that neutrinos possess non-zero masses, highlighting a limitation in the SM.

Strong CP problem: CP, which stands for "charge conjugation and parity inversion," refers to processes involving the reversal of charge and parity properties. The Strong CP Problem is a challenge in QCD, a theory describing the strong force interactions among quarks and gluons. The problem revolves around the θ (theta) term in QCD, which is a parameter describing the vacuum structure of the theory and has the potential to introduce violations of both parity (P) and charge conjugation (C). If the θ term takes on a large value, it leads to significant electric dipole moments for particles like neutrons and protons, which contradicts the observed values. The Strong CP Problem thus raises the question of why the θ term is so small or effectively zero, given the physical observations.

One proposed solution to this problem involves a symmetry known as the Peccei-Quinn symmetry, which alters the nature of the action and renders the θ term ineffective or significantly reduces its impact. This symmetry results in a scenario where the observed parity and charge are conserved. The Peccei-Quinn symmetry (18) introduces a hypothetical particle called the axion. Axions (19) are pseudoscalar particles that arise as a consequence of the spontaneous breaking of the Peccei-Quinn symmetry. These particles play a crucial role in resolving the Strong CP Problem by dynamically adjusting the θ (theta) term to a very small or effectively zero value, thus preventing the violation of CP symmetry. However, a complete solution has not yet been found, and the Strong CP Problem remains a topic of ongoing exploration by particle physicists.

Grand Unified Theories (GUTs): GUTs aims to unify the electromagnetici weak, strong forces into a single theoretical framework. According to GUTs, these forces were once a single force in the early universe but later separated as the universe cooled. GUTs suggest that at extremely high energies, the unified force undergoes a process of spontaneous symmetry breaking, leading to the distinct forces we observe today. GUTs predict the existence of magnetic monopoles, theoretical particles possessing a single magnetic pole. Despite extensive searches, these particles have eluded direct observation, posing a significant challenge to the GUT framework. One significant prediction of GUTs is the possibility of proton decay. According to GUTs, protons, a seemingly stable particle in the SM, may undergo decay process. While experiments have set stringent constraints on the proton's lifetime, no definitive observation of proton decay has been made to date.

Supersymmetry (SUSY): SUSY posits a fundamental symmetry bridging bosons and fermions within the Standard Model. According to SUSY, every known particle has a supersymmetric partner, distinguished by a spin difference of half a unit. Each known particle has a supersymmetric partner, differing in spin by half a unit. The supersymmetric particles, like selectrons and photinos, are being sought in experiments at accelerators like the LHC. Despite extensive searches, no direct evidence has been found, constraining potential supersymmetric particles masses. The lightest supersymmetric particle (LSP) (20), frequently identified as a neutralino, emerges as a compelling candidate for dark matter. This is attributed to its stability and weak interaction characteristics. The exploration of Supersymmetry offers insights into the hierarchy problem and may provide solutions to longstanding questions in particle physics.

Many of these theories predict the existaence of undiscovered phenomena that extend beyond the boundaries of the SM. The investigation of BSM theories transcends mere intellectual pursuit, carrying tangible implications for our comprehension of the cosmos. These theories are instrumental in addressing enigmas like dark matter and dark energy, while also aspiring to provide a unified description of fundamental forces. BSM theories pave the way for a more comprehensive and elegant understanding of the universe. Current experiments and advancements in particle physics are dedicated to scrutinizing these predictions, expanding the frontiers of our knowledge and ushering in the next epoch in fundamental physics.

1.3 Effective Field Theories

Although the Standard Model has successfully explained many experimental findings, it's important to recognize that its applicability may have limits, represented by an unknown energy scale denoted as Λ. As we explore energy scales beyond Λ, the scattering amplitudes resulting from EFT (21) operators quickly increase, eventually unitarity violation (UV) in a way considered unrealistic. This phenomenon is comprehensively understood within the realm of EFT, and various strategies are employed to address and decrease these divergences. Techniques such as incorporating ad-hoc form factors, employing clipping procedures, or implementing K-matrix unitarization are commonly utilized to manage and regularize the behavior of scattering amplitudes in these high-energy scenarios. These techniques as a tool to parameterize the impact of high-energy physics on low-energy phenomena, effectively introducing additional degrees of freedom beyond those accounted for in the SM. Yet, delving into the intricacies of the interactions involving dimensional-8 anomalous quartic operators and the neutral gauge bosons (γ and Z) within the framework of EFT is a highly intricate and theoretical endeavor. EFT eases this complexity by incorporating higher-dimensional operators (HDO) and their associated coefficients. This inclusion permits a systematic expansion of the Lagrangian, enabling a comprehensive approach to capturing deviations from SM predictions. Anomalous quartic gauge couplings come out as a result of dimension-8 operators. Anomalous quartic gauge couplings can be expressed using either linear or non-linear representations within the framework of EFT. In the linear representation, the breaking of electroweak symmetry occurs through the conventional Standard Model Higgs mechanism.

On the contrary, within the non-linear representation, Higgs couplings are treated as supplementary free parameters. Given the absence of observed deviations from the predictions of the light Standard Model Higgs, a more cautious approach involves exploring an effective Lagrangian in a model-independent model for the aQGCs. This approach assumes that any potential NP beyond the Standard Model upholds $SU(2)_L \times U(1)$ gauge invariance within the linear representation (22,23-25).

Dimension-8 operators are classified into three groups: the first encompasses covariant derivatives of the Higgs doublet exclusively ($\mathcal{O}_{S,j}$), the second involves two field strength tensors and two derivatives of the Higgs doublet ($\mathcal{O}_{M,j}$), and the third comprises field strength tensors only ($\mathcal{O}_{T,j}$). Consequently, these three classes of dimension-8 effective operators are integrated into the SM Lagrangian. This expanded Lagrangian accommodates deviations from the aQGCs, providing a framework for investigating potential NP effects beyond the SM.

The Lagrangian characterizing the dimension-8 operators that contribute to anomalous quartic gauge couplings can be articulated in the following manner,

$$\mathcal{L}_{eff} = \mathcal{L}_{SM} + \sum_i \frac{c_i}{\Lambda^2} \mathcal{O}_i \qquad (1.1)$$

$$\mathcal{L}_{eff} = \mathcal{L}_{SM} + \sum_{j=0}^{1} \frac{f_{S,j}}{\Lambda^4} \mathcal{O}_{S,j} + \sum_{j=0}^{7} \frac{f_{M,j}}{\Lambda^4} \mathcal{O}_{M,j} + \sum_{\substack{j=0 \\ j\neq 3}}^{9} \frac{f_{T,j}}{\Lambda^4} \mathcal{O}_{T,j} \qquad (1.2)$$

Λ stands for the scale at which new physics becomes significant, and $f_{S,j}$, $f_{M,j}$, and $f_{T,j}$ are the coefficients associated with the related effective operators. These coefficients are zero within the SM predictions.

References (22,23-25) contain the detailed expressions for the 18 quartic gauge operators at dimension-8. The expression of dimension-8 operators contributing to anomalous quartic gauge couplings is as follows,

$$O_{S0} = \left[(D_\mu\Phi)^\dagger D_\nu\Phi\right] \times \left[(D^\mu\Phi)^\dagger D^\nu\Phi\right], \qquad O_{T0} = Tr\left[\widehat{W}_{\mu\nu}\widehat{W}^{\mu\nu}\right] \times Tr\left[\widehat{W}_{\alpha\beta}\widehat{W}^{\alpha\beta}\right]$$

$$O_{S1} = \left[(D_\mu\Phi)^\dagger D^\mu\Phi\right] \times \left[(D_\nu\Phi)^\dagger D^\nu\Phi\right], \qquad O_{T1} = Tr\left[\widehat{W}_{\alpha\nu}\widehat{W}^{\mu\beta}\right] \times Tr\left[\widehat{W}_{\mu\beta}\widehat{W}^{\alpha\nu}\right]$$

$$O_{S2} = \left[(D_\mu\Phi)^\dagger D_\nu\Phi\right] \times \left[(D^\nu\Phi)^\dagger D^\mu\Phi\right], \qquad O_{T2} = Tr\left[\widehat{W}_{\alpha\mu}\widehat{W}^{\mu\beta}\right] \times Tr\left[\widehat{W}_{\beta\nu}\widehat{W}^{\nu\alpha}\right]$$

$$O_{M0} = Tr\left[\widehat{W}_{\mu\nu}\widehat{W}^{\mu\nu}\right] \times \left[(D_\beta\Phi)^\dagger D^\beta\Phi\right], \qquad O_{T5} = Tr\left[\widehat{W}_{\mu\nu}\widehat{W}^{\mu\nu}\right] \times \hat{B}_{\alpha\beta}\hat{B}^{\alpha\beta}$$

$$O_{M1} = Tr\left[\widehat{W}_{\mu\nu}\widehat{W}^{\mu\beta}\right] \times \left[(D_\beta\Phi)^\dagger D^\mu\Phi\right], \qquad O_{T6} = Tr\left[\widehat{W}_{\alpha\nu}\widehat{W}^{\mu\beta}\right] \times \hat{B}_{\mu\beta}\hat{B}^{\alpha\nu} \tag{1.3}$$

$$O_{M2} = \left[\hat{B}_{\mu\nu}\hat{B}^{\mu\nu}\right] \times \left[(D_\beta\Phi)^\dagger D^\beta\Phi\right], \qquad O_{T7} = Tr\left[\widehat{W}_{\alpha\mu}\widehat{W}^{\mu\beta}\right] \times \hat{B}_{\beta\nu}\hat{B}^{\nu\alpha}$$

$$O_{M3} = \left[\hat{B}_{\mu\nu}\hat{B}^{\nu\beta}\right] \times \left[(D_\beta\Phi)^\dagger D^\mu\Phi\right] \qquad O_{T8} = \left[\hat{B}_{\mu\nu}\hat{B}^{\mu\nu}\,\hat{B}_{\alpha\beta}\hat{B}^{\alpha\beta}\right]$$

$$O_{M4} = \left[(D_\mu\Phi)^\dagger\,\widehat{W}_{\beta\nu}\,D^\mu\Phi\right] \times \hat{B}^{\beta\nu} \qquad O_{T9} = \left[\hat{B}_{\alpha\mu}\hat{B}^{\mu\beta}\,\hat{B}_{\beta\nu}\hat{B}^{\nu\alpha}\right]$$

$$O_{M5} = \left[(D_\mu\Phi)^\dagger\,\widehat{W}_{\beta\nu}D^\nu\Phi\right] \times \hat{B}^{\beta\nu} + h.c.,$$

$$O_{M7} = \left[(D_\mu\Phi)^\dagger\,\widehat{W}_{\beta\nu}\widehat{W}^{\beta\mu}D^\nu\Phi\right].$$

Where field strength tensors for SU(2) ($W_{\mu\nu}$) and U(1) ($B_{\mu\nu}$) are provided as

$$W_{\mu\nu} = \frac{i}{2} g\tau^i\left(\partial_\mu W_\nu^i - \partial_\nu W_\mu^i + g\epsilon_{ijk}W_\mu^j W_\nu^k\right) \tag{1.4}$$

$$B_{\mu\nu} = \frac{i}{2} g'\left(\partial_\mu B_\nu - \partial_\nu B_\mu\right) \tag{1.5}$$

Here, τ^i (i = 1, 2, 3) represent the generators of SU(2), g is defined as $e/sin\theta_W$, g' is expressed as $g/cos\theta_W$, where e denotes the elementary electric charge, and θ_W stands for the Weinberg angle.

Table 1.1. Highlights quartic gauge boson vertices influenced by their respective dimension-8 operators, denoted with a checkmark '✓'.

	WWWW	WWZZ	ZZZZ	WWγZ	WW$\gamma\gamma$	ZZZγ	ZZ$\gamma\gamma$	Z$\gamma\gamma\gamma$	$\gamma\gamma\gamma\gamma$
$\mathcal{O}_{S0}, \mathcal{O}_{S1}$	✓	✓	✓						
$\mathcal{O}_{M0}, \mathcal{O}_{M1}, \mathcal{O}_{M6}, \mathcal{O}_{M7}$	✓	✓	✓	✓	✓	✓	✓		
$\mathcal{O}_{M2}, \mathcal{O}_{M3}, \mathcal{O}_{M4}, \mathcal{O}_{M5}$		✓	✓	✓	✓	✓	✓		
$\mathcal{O}_{T0}, \mathcal{O}_{T1}, \mathcal{O}_{T2}$	✓	✓	✓	✓	✓	✓	✓	✓	✓
$\mathcal{O}_{T5}, \mathcal{O}_{T6}, \mathcal{O}_{T7}$		✓	✓	✓	✓	✓	✓	✓	✓
$\mathcal{O}_{T8}, \mathcal{O}_{T9}$			✓			✓	✓	✓	✓

Table 1.1 provides a comprehensive catalog of quartic gauge boson vertices altered by dimension-8 operators. Signal process of pp → γγγ is analyzed by exploiting the inherent phase space characteristics, achieving optimal sensitivity to anomalous quartic couplings related to γγγZ and γγγγ vertices. As only operators of the field strength tensor type ($\mathcal{O}_{T,x}$) contribute to the quartic vertices $\gamma\gamma\gamma Z$ and $\gamma\gamma\gamma\gamma$, we choose the $\mathcal{O}_{T,8}$ and $\mathcal{O}_{T,9}$ couplings to encompass all variations of $\mathcal{O}_{T,x}$ operators.

The anomalous quartic $\gamma\gamma\gamma Z$ and $\gamma\gamma\gamma\gamma$ vertices are expressed as a function of f_{T8}/Λ^4 and f_{T8}/Λ^4 couplings as follows

$$\Gamma^{\mu\nu\alpha\beta}_{\gamma\gamma\gamma Z}(p_1, p_2, p_3, p_4) = -8 s_W c_W^3 \left[4\frac{f_{T8}}{\Lambda^4} G(f_{T8}) + \frac{f_{T9}}{\Lambda^4} G(f_{T9})\right] \quad (1.6)$$

$$\Gamma^{\mu\nu\alpha\beta}_{\gamma\gamma\gamma\gamma}(p_1, p_2, p_3, p_4) = 8 c_W^4 \left[4\frac{f_{T8}}{\Lambda^4} G(f_{T8}) + \frac{f_{T9}}{\Lambda^4} G(f_{T9})\right] \quad (1.7)$$

The sine (cosine) of the weak mixing angle (θ_W,) is denoted by s_W (c_W), while G(f_{T8}) and G(f_{T9}) are defined as follows;

$$\begin{aligned} G(f_{T8}) = {} & (p_1.p_2)\Big[g^{\mu\nu}\Big(g^{\alpha\beta}(p_3.p_4) - p_3^{\beta}p_4^{\alpha}\Big)\Big] - (p_3.p_4)g^{\alpha\beta}p_1^{\nu}p_3^{\mu} + p_1^{\nu}p_2^{\mu}p_3^{\beta}p_4^{\alpha} + p_1^{\beta}p_2^{\alpha}p_3^{\nu}p_4^{\mu} \\ & + p_1^{\alpha}p_2^{\beta}p_3^{\mu}p_4^{\nu} + \Big[(p_1.p_3)g^{\mu\alpha}\Big(g^{\nu\beta}(p_2.p_4) - p_2^{\beta}p_4^{\alpha}\Big) - (p_2.p_3)g^{\nu\alpha}p_1^{\beta}p_4^{\mu})\Big] + [p_3 \leftrightarrow p_4, \alpha \leftrightarrow \beta] \end{aligned} \quad (1.8)$$

$$\begin{aligned} G(f_{T9}) = {} & (p_1.p_2)[g^{\mu\alpha}\Big(g^{\nu\beta}(p_3.p_4) - p_3^{\beta}p_4^{\nu}\Big) + g^{\mu\beta}(g^{\nu\alpha}(p_3.p_4) - p_3^{\nu}p_4^{\alpha}) + g^{\alpha\beta}(p_3^{\nu}p_4^{\mu} + p_3^{\mu}p_4^{\nu}) \\ & - g^{\nu\beta}p_3^{\mu}p_4^{\alpha} - g^{\nu\alpha}p_3^{\beta}p_4^{\mu}\Big] + (p_3.p_4)\Big[g^{\mu\nu}\Big(p_1^{\beta}p_2^{\alpha} + p_1^{\alpha}p_2^{\beta}\Big) - g^{\mu\beta}p_1^{\nu}p_2^{\alpha} - g^{\mu\alpha}p_1^{\nu}p_2^{\beta} - g^{\nu\beta}p_1^{\alpha}p_2^{\mu} \\ & - g^{\nu\alpha}p_1^{\beta}p_2^{\mu}\Big] + p_1^{\nu}p_2^{\beta}p_3^{\mu}p_4^{\alpha} + p_1^{\nu}p_2^{\alpha}p_3^{\beta}p_4^{\mu} + p_1^{\beta}p_2^{\mu}p_3^{\nu}p_4^{\alpha} + p_1^{\beta}p_2^{\alpha}p_3^{\mu}p_4^{\nu} + p_1^{\alpha}p_2^{\beta}p_3^{\nu}p_4^{\mu} + p_1^{\alpha}p_2^{\mu}p_3^{\beta}p_4^{\nu} \\ & + [(p_1.p_3)[g^{\alpha\beta}(g^{\mu\nu}(p_2.p_4) - p_2^{\mu}p_4^{\nu}) + g^{\mu\beta}(g^{\nu\alpha}(p_2.p_4) - p_2^{\alpha}p_4^{\nu}) + g^{\nu\beta}(p_2^{\mu}p_4^{\alpha} + p_2^{\alpha}p_4^{\mu}) \\ & - g^{\mu\nu}p_2^{\beta}p_4^{\alpha} - g^{\nu\alpha}p_2^{\beta}p_4^{\mu}\Big] + (p_2.p_3)\Big[g^{\mu\beta}(p_1^{\nu}p_4^{\alpha} + p_1^{\alpha}p_4^{\nu}) - g^{\mu\nu}p_1^{\beta}p_4^{\alpha} - g^{\nu\beta}p_1^{\alpha}p_4^{\mu} - g^{\alpha\beta}p_1^{\nu}p_4^{\mu} \\ & - g^{\mu\alpha}p_1^{\beta}p_4^{\nu}\Big]\Big] + [p_3 \leftrightarrow p_4, \alpha \leftrightarrow \beta] \end{aligned} \quad (1.9)$$

The most recent experimental limitations on aQGCs, specifically f_{T8}/Λ^4 and f_{T9}/Λ^4, have been derived by the CMS and ATLAS collaborations. These constraints were obtained at a center-of-mass energy of 13 TeV, utilizing an integrated luminosity of 137 and 139 fb^{-1} at the LHC. The investigation involved the analysis of Vector Boson Scattering (VBS) and tri-boson production channels. In these examinations, the tri-boson production channel is approached as the production of a Z boson in association with two photons. Meanwhile, the VBS production channel is characterized as the electroweak production of a Z boson, a photon, and two forward jets, or alternatively, the electroweak production of two jets and a pair of Z bosons. The Z-boson decay, manifesting as two charged leptons ($Z \rightarrow ll$) or two neutrinos ($Z \rightarrow \nu\nu$), results in distinct final states within both production channels.

The determined limit values, not accounting for unitarity preservation, on f_{T8}/Λ^4 and f_{T9}/Λ^4 by the ATLAS and CMS collaborations are presented in Table 1.2. The most stringent experimental limits at a 95% Confidence Level (C.L.) on f_{T8}/Λ^4 and f_{T9}/Λ^4 stem from the analysis of electroweak Z(νν)γ production in association with two jets conducted by the ATLAS collaboration at a center-of-mass energy of 13 TeV, utilizing an integrated luminosity of 139 fb^{-1} (26).

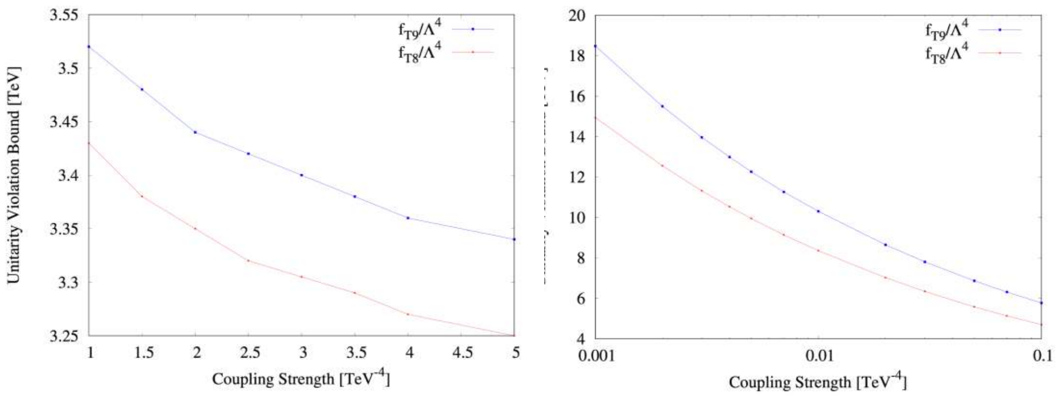

Figure 1.2. The unitarity violation bound for aQGCs f_{T8} and f_{T9} for HL-LHC ($\sqrt{s} = 14\ TeV$) and FCC-hh ($\sqrt{s} = 100\ TeV$) colliders.

As previously mentioned, the applicability of effective field theory is confined to the domain of the new physics scale, where unitarity violation remains absent. Nevertheless, the presence of HDO, characterized by nonzero aQGC, introduces the potential for a scattering amplitude to breach unitarity at sufficiently elevated energy levels. This critical threshold is denoted as the unitarity bound.

The determination of the unitarity bound for dimension-8 operators involves the utilization of a dipole form factor, designed to uphold unitarity at high energies. This is expressed as:

$$FF = \frac{1}{(1+\hat{s}/\Lambda_{FF}^2)^2} \tag{1.10}$$

where $\hat{s}$ is denoted as the partonic center of mass energy, serves as the maximum energy scale, and ΛFF signifies the cut-off scale for the form factor. The determination of the maximal form factor scale, ΛFF, was carried out through the utilization of the form factor tool Vector Boson Fusion Next-to-Leading-Order (VBFNLO) 2.7.1 (27) version, considering a specified set of input parameters for anomalous quartic gauge boson couplings. VBFNLO is a versatile partonic Monte Carlo program designed for achieving NLO QCD accuracy in vector boson fusion, as well as double and triple vector boson production processes.

The determination of the form factor in the VBFNLO tool involves analyzing the amplitudes of on-shell VV scattering processes and calculating the zeroth partial wave of the amplitude. Adhering to the unitarity criterion, the real part of the zeroth partial wave must not exceed 0.5. This criterion is consistently applied across all channels with the same electrical charge Q in VV → VV scattering (V=W/Z/γ). Additionally, individual checks are conducted for each channel within the VV system. Figure 1.2 illustrates the UV bounds calculated using the form factor tool with VBFNLO at HL-LHC and FCC-hh energies., corresponding to the higher-dimensional operators considered in our study. The boundaries depict the regions associated with each coefficient's line, ensuring that unitarity is maintained below these lines. This sheds light on the constraints applied to these couplings at different collision energies.

Table 1.2. The UV boundaries of aQGCs, denoted as f_{T8}/Λ^4 and f_{T9}/Λ^4 in on-shell VV (V=W/Z/γ) scattering processes.

Channels	$f_{T8}/\Lambda^4 (TeV^{-4})$	$f_{T9}/\Lambda^4 (TeV^{-4})$	$\sqrt{s}$ (TeV)	L_{int} (fb^{-1})	Collabration
$Z(ll)\gamma\gamma$	[-1.06;1.10]	[-1.82;1.82]	13	137	CMS (28)
$Z(ll)Z(ll)jj$	[-0.43;0.43]	[-0.92;0.92]	13	137	CMS (29)
$Z(ll)\gamma jj$	[-0.47;0.47]	[-0.91;0.91]	13	137	CMS (30)
$Z(\nu\bar{\nu})\gamma jj$	[-0.059;0.059]	[-0.13;0.13]	13	139	ATLAS (26)

2. THE FUTURE HADRON-HADRON COLLIDER PROJECTS

Particle colliders have played a pivotal role in unraveling the mysteries of sub-atomic world. While existing accelerators continue to operate, collect valuable data, and offer insights, preparations for the next generation of experiments are already underway. This process spans several years and involves defining objectives, addressing challenges, pioneering new technologies, and ensuring that these proposed experiments have the potential to advance our understanding. The hadron collider is an intricately complex apparatus, with the primary emphasis in design placed on the accelerator.

In this context, the LHC located in the city of Geneva, Switzerland, under the auspices of the European Organization for Nuclear Research (CERN), stands as the world's largest and most powerful circular proton-proton collider. The primary goal of the LHC is to investigate high-energy physics and seek answers to questions related to the Standard Model. The maximum achievable energy is directly related to the size of the accelerator. Therefore, the LHC has been constructed in a 27-kilometer circular tunnel using superconducting magnets. In recent decades, particle physics detectors also have witnessed significant performance improvements. The development of large-scale detector structures and access to a highly advanced silicon industry with exponential performance growth has paved the way for increasingly sophisticated detectors. Examples of these state-of-the-art detectors include those used in the LHC experiments, such as ALICE, ATLAS, CMS, and LHCb. These four different detectors house a variety of experiments in high-energy physics. ATLAS and CMS detectors operate at high brightness, while ALICE and LHCb collect data at low brightness. Figure 2.1 illustrates the schematic of the LHC, outlining the configuration of the four collision points.

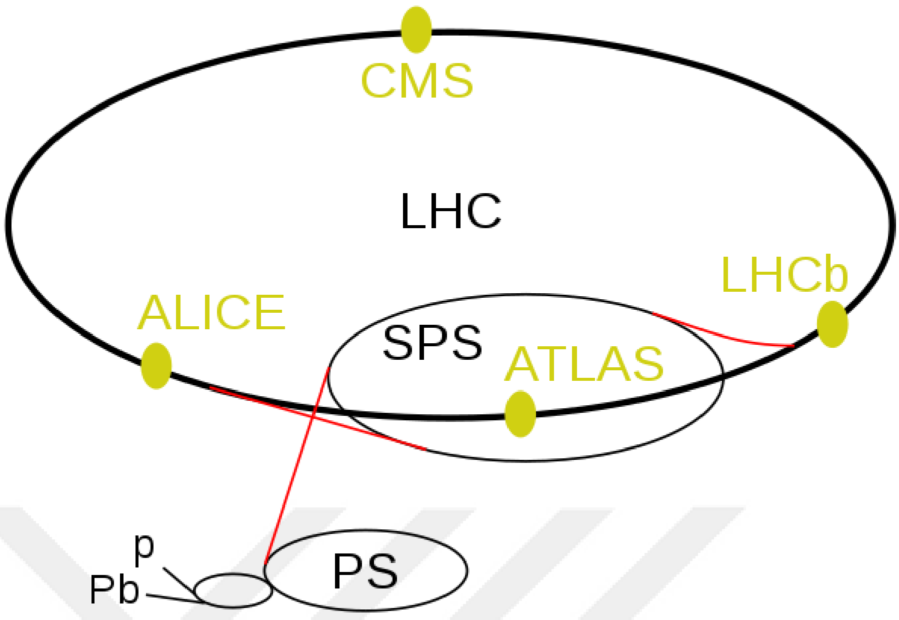

Figure 2.1. A schematic view of LHC (31).

The LHC is designed to collide particle and proton beams at a center-of-mass energy of 14 TeV and is capable of accommodating up to 10^{11} particles with a projected design luminosity of $10^{34} cm^{-2} s^{-1}$. These resulting beams are accelerated by more than 9000 superconducting magnets to be measured in four main detectors.

The rate of beam-beam collision events per second for a particular process can be calculated using:

$$\frac{dN}{dt} = \sigma . L \quad (2.1)$$

where σ is the cross-section of the process, and L is the instantaneous luminosity. Luminosity is a parameter that varies depending on the machine and can be customized to suit the experimental needs. The maximum energy and luminosity that can be achieved are the most crucial design parameters for a particle physics accelerator.

The LHC has undergone two distinct operational phases to date. The first phase, which spanned from 2008 to 2013, featured proton-proton collisions with a collision energy of $\sqrt{s}$ = 8 TeV. The second phase, occurring between 2015 and 2018, witnessed collisions at an energy of $\sqrt{s}$ = 13 TeV. The ongoing third phase, initiated in 2022 and anticipated to continue until 2026, is characterized by a collision energy of $\sqrt{s}$ = 13.6 TeV. The upcoming fourth phase, slated for 2029, is set to achieve a collision energy of $\sqrt{s}$ = 14 TeV, accompanied by substantially increased luminosity. The primary objectives of the LHC encompass the exploration of the TeV energy range, the investigation of the Higgs Boson, and the pursuit of potential new physics phenomena, all within the framework of the Standard Model. Figure 2.2 provides a detailed map of the transition process from the LHC to the HL-LHC.

Figure 2.2. A scheme of HL-LHC plan (32).

The identification of the Higgs boson in 2012 by the ATLAS and CMS collaborations marked a crucial achievement, closely aligning with anticipated outcomes based on unitarity principles. This breakthrough signified that the experiments conducted at the Large Hadron Collider (LHC) were aptly positioned to delve into the complex origins of electroweak symmetry breaking which involves the conversion of the $SU(2)_L \times U(1)$ gauge symmetry into the $U(1)$ of electromagnetism.

As we advance in our scientific journey, it has become increasingly evident that the properties and behavior of the Higgs boson closely match the predictions set forth by the Standard Model. However, our quest for deeper understanding encounters a compelling challenge the absence of direct signals from BSM particles. This enigma has prompted the scientific community to recognize the pressing necessity for a higher-energy collider like the HL-LHC.

The HL-LHC's significance lies in its capacity to propel humanity further into the profound mysteries of particle physics, potentially serving as the bridge that connects the familiar terrain of the known particle spectrum within the Standard Model with the uncharted territories of BSM physics, where new and transformative insights await.

2.1 HL-LHC

The HL-LHC, represents a remarkable leap forward in the field of high-energy particle physics. Situated at the European Organization for Nuclear Research (CERN) on the border of Switzerland and France, this state-of-the-art facility is slated to usher in a new era of scientific exploration and discovery. The HL-LHC project is a remarkable upgrade to the LHC, the world's most powerful particle accelerator. Its primary goal is to dramatically increase the luminosity of the LHC, aiming for a five to sevenfold increase compared to its original design. This heightened luminosity will provide scientists with an abundance of data, resulting in a much deeper and statistically more significant understanding of the fundamental building blocks of our universe.

The HL-LHC is set to enhance our ability to explore the mysteries of particle physics, going beyond the boundaries of the Standard Model, which has served as the foundation of our understanding for decades. It will facilitate precision measurements of known particles, search for new physics phenomena, and provide insight into some of the most profound questions in the field. The High-Luminosity

LHC is set to deliver proton-proton collisions at 14 TeV to the CMS and ATLAS experiments, offering a substantial integrated luminosity of approximately 3000 fb^{-1}. However, achieving the highest attainable peak luminosity is a formidable challenge, influenced by various factors. Among these challenges, the issue of pile-up events during each bunch crossing is of utmost concern, as these events can significantly impact the quality of data collected for rigorous physics analysis. In response to this challenge, the High-Luminosity LHC has implemented a meticulous strategy, maintaining a constant instantaneous luminosity that does not exceed $5 \times 10^{34} cm^{-2}s^{-1}$. This precisely controlled luminosity equates to an average of approximately 140 events per bunch crossing when operating with a 25 ns bunch spacing.

The HL-LHC stands as a testament to international collaboration and the unrelenting human quest for knowledge. Researchers from all corners of the globe are uniting to push the boundaries of our understanding of the universe. As the HL-LHC continues to develop and takes its place on the frontiers of scientific discovery, it stands as a testament to human ingenuity and our unceasing curiosity about the cosmos. This cutting-edge facility promises to open new doors to knowledge and pave the way for groundbreaking discoveries that will reshape our understanding of the universe.

2.2 FCC-hh

The FCC takes the form of a circular ring, akin to the LHC, covering a perimeter of approximately 100 kilometers. Despite not having undergone physical testing, simulations, and detector effect cards provide the means to replicate interactions between collisions. The primary challenge faced by detectors at future hadron colliders stems from the substantial increase in luminosity. The FCC facility is poised to become the most potent infrastructure in particle physics, succeeding the LHC, by tackling the critical unresolved questions in the field. The FCC has three phases which are FCC-ee, FCC-hh, and FCC-he. The FCC-hh represents a groundbreaking particle accelerator project engineered for proton-proton collisions. Beyond its role in precision testing of the Standard Model (SM) and Beyond

Standard Model (BSM) theories, the FCC-hh is poised to explore some of the universe's most profound mysteries, including dark energy and dark matter. The second phase of the FCC integrated program builds on a high-energy collider, FCC-hh, with an integrated luminosity of a factor of 5-10 larger than the HL-LHC and a thirty-fold increase compared to the LHC. Also, it has a consistent bunch spacing of 25 ns as the LHC. The FCC-hh boasts an astounding center-of-mass energy of 100 TeV and a remarkable integrated luminosity of 30 ab −1, designed to operate continuously for a span of 25 years. The shift from the HL-LHC to the FCC-hh, with an escalation in energy level from 14 to 100 TeV, results in a 1.75-fold increase in the number of charged particles per pp collision. Consequently, the primary cause of the elevated hit rate and data rate when transitioning from HL-LHC to FCC-hh is predominantly the amplified luminosity.

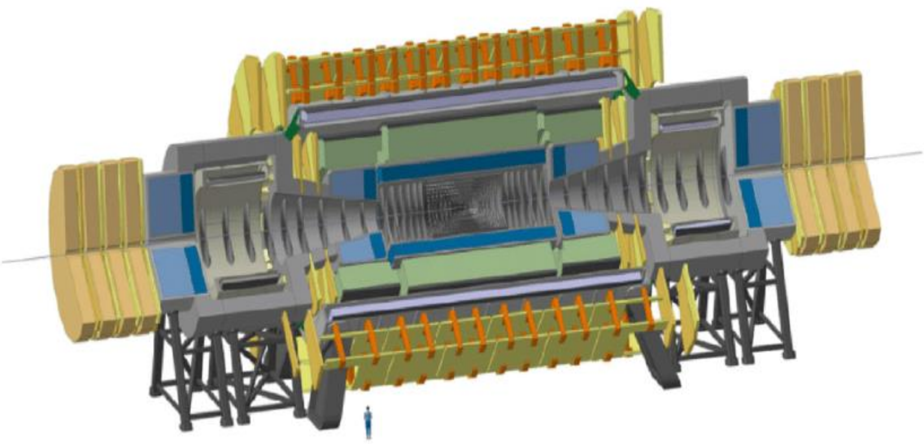

Figure 2.3. The FCC-hh Reference Detector: Layout Overview (33).

Figure 2.3 presents a detailed cross-sectional view of the FCC-hh reference detector, offering a comprehensive depiction of its internal structure and components. This visual representation is a practical model that helps researchers study subsystems and various physics aspects. It highlights areas where additional research and development efforts are necessary. However, it doesn't provide a detailed technical design for practical use. The reference detector configuration includes the central region housed within a 4T solenoid with a 10-meter inner cavity diameter, ensuring coverage of $|\eta| < 2.5$. Simulation studies predict that new physics events will occur in the forward region ($|\eta| > 2.5$). To achieve the required performance, the forward regions of the reference detector are shifted 10 meters along the beam axis from the interaction point. Two forward magnet coils, featuring a 5-meter inner bore, supply the required bending power. Functioning as solenoids with a 4T field, these forward magnets contribute to a total solenoid volume extending over 32 meters in length. This design facilitates high-precision momentum spectroscopy up to $|\eta| \approx 4$ and tracking capabilities up to $|\eta| \approx 6$. As a result, the overall length of the detector spans approximately 50 meters with a diameter of 20 meters, positioning it in a size range comparable to the ATLAS detector at the LHC. The FCC-hh reference detector is mandated to possess advanced capabilities for the precise measurement of particles within its experimental setting. The FCC-hh incorporates a silicon-based tracking system characterized by a 1.6-meter radius and an overall length of 30 meters. Designed to deliver accurate measurements for particles with low momentum, this tracking system achieves a resolution of approximately 0.6% for low-momentum particles, 2% at 1 TeV, and 20% at 10 TeV.

FCC-hh magnets play a critical role in steering and focusing particle beams, enabling them to circulate and collide at high energies. These magnets are essential components of the accelerator ring. They need to be capable of withstanding the high energies and magnetic fields involved, while also maintaining superconducting properties to minimize energy losses. There are various types of magnets used in the FCC-hh, including 16T superconducting Dipole Magnets: These are responsible for bending the particle beams, keeping them in a circular path. The FCC-hh will require large superconducting dipole magnets to achieve the necessary bending and focusing of the beams.

When proton collisions transpire at unparalleled center-of-mass energies, they generate particles with energies reaching into the multi-TeV range. The energy measurement in calorimeters, being inherently statistical, exhibits an enhanced resolution with increasing energy levels. This characteristic renders calorimeters an ideal selection for accurately measuring particles with energies situated in the multi-TeV range. The calorimetry system in FCC-hh encompasses both electromagnetic calorimeters (ECAL) and hadronic calorimeters (HCAL), following a design reminiscent of other high-energy physics experiments such as the LHC and the ATLAS detector. The baseline detector's calorimetry design draws inspiration from the ATLAS detector. However, an alternative has been introduced for the central electromagnetic system, utilizing silicon sensors. Nevertheless, this alternative is not suitable for the endcap and forward regions due to high radiation levels. For the central electromagnetic calorimeter and the combined calorimetry in the endcaps and forward regions, the established design relies on liquid argon. In the central region, the hadronic calorimeter employs scintillator tiles, offering significantly increased granularity compared to the ATLAS detector. The enhanced granularity in the central electromagnetic calorimeter is made possible through the use of straight multilayer electrodes, while the hadronic calorimeter benefits from silicon photomultipliers.

The FCC facility is poised to become the most potent infrastructure in particle physics, succeeding the LHC, by tackling the critical unresolved questions in the field.

3. AIM AND SCOPE OF THE STUDY

This thesis sets out to explore the intricate dynamics of gauge boson self-interactions within the SM, with a primary aim of identifying deviations from the expected behaviors. The central theme revolves around comprehending the self-couplings guided by non-Abelian gauge symmetry and investigating potential indications of NP beyond the Standard Model.

The study employs an effective field theory approach for the systematic adjustment of self-interactions, with a specific emphasis on anomalous quartic gauge dimension-8 couplings related to γγγγ and γγγZ vertices. The investigation focuses on the tri-photon production process, aiming to extract valuable insights into the underlying physics.

Expanding the investigation, the study delves into upcoming hadron colliders, notably the HL-LHC operating at 14 TeV and the FCC-hh at 100 TeV. Integrated luminosities of 3 ab^{-1} for HL-LHC and 30 ab^{-1} for FCC-hh are taken into consideration.

To attain the outlined objectives, the study involves event generation, accounting for parton showering and detector effects. Both traditional Monte Carlo methods and contemporary machine learning techniques, particularly the Toolkit for Multivariate Data Analysis with ROOT (TMVA) using Boosted Decision Trees, are employed for event analysis.

In summary, this thesis aims to make significant contributions to our understanding of gauge boson self-couplings and potential deviations from SM predictions. Through a comprehensive analysis across current and future high-energy hadron colliders, the research anticipates shedding light on NP beyond the established boundaries of the Standard Model.

4. MATERIALS AND METHODS

The investigation of anomalous quartic dimension-8 couplings related to $\gamma\gamma\gamma\gamma$ and $\gamma\gamma\gamma Z$ vertices in tri-photon production at future hadron colliders is a focal point of our study. In this section, we depend on Monte Carlo (34) method, a vital tool in our research methodology, to thoroughly analyze outcomes. These methods enable us to generate events, simulate outcomes, predict uncertainties in our experimental results, and calculate systematic variations with precision.

A pivotal tool employed for this objective is MadGraph (35), a broadly utilized Monte Carlo event generator based on general-purpose matrix elements. It plays an important role in simulating events within the particle colliders as part of modern scientific research. MadGraph's strength lies in its extraordinary versatility, allowing seamless extensions and adaptability to a wide range of experimental scenarios. The successful solution to the challenge of automatically generating tree-level matrix elements encompasses a broad spectrum of renormalizable models. This achievement transcends the conventional realm of Feynman diagrams and relies on the adept utilization of efficient multiparton techniques. This progress has been made possible by standardizing communication between FeynRules and matrix element programs, achieved through the introduction of a groundbreaking Universal FeynRules Output format commonly known as UFO (36). This versatile tool is capable of producing tree-level matrix elements for a diverse array of Lagrangian-based models, whether they are renormalizable or effective, and these models are implemented within FeynRules through the UFO interface.

In the context of hadron colliders, where interactions involving primary particles such as gluons and quarks occur at the parton level, Parton Distribution Functions (PDF) are commonly used to characterize the initial four momentum of these interactions. MadGraph also includes Pythia (37), a powerful random event generator, and integrates seamlessly with Pythia code, including matrix element evaluation, parton shower, hadronization, particle decays, and basic event modeling. Additionally, MadGraph interfaces seamlessly with a major detector simulator, Delphes, further increasing its usefulness. The Delphes (38) framework comprehensively simulates the response of the detector, consisting of an internal tracker, electromagnetic and hadron calorimeters, and a muon system. All these components are thoughtfully arranged with cylindrical symmetry around the beam axis. It has the flexibility to determine parameters such as the active volume of the detector, calorimeter segmentation, and the strength of the uniform magnetic field.

As a result of this simulation, the resultant particles undergo reconstruction while considering genuine detector effects and are subsequently processed for physics objects through the application of algorithms such as isolation, tagging, and FastJet. The simulation outcome, comprising final state particles like photons, muons, and jets, is then documented in a root file for later offline analysis. In summary, Delphes facilitates the swift and straightforward generation of the desired physics processes, while also incorporating lifelike detector effects. This versatility allows Delphes to adapt it to a wide variety of collider experiments, facilitating precise and effective data analysis. Depending on the nature of our simulation goals, some of these additional components may prove unnecessary. For instance, if our goal is to compute a cross-section solely at the parton level, the basic MadGraph software is often sufficient. It provides a solid foundation for these computations. However, when we aim to delve deeper into the simulation, encompassing processes like hadronization or simulating the detector response, we must incorporate additional elements such as Pythia and Delphes.

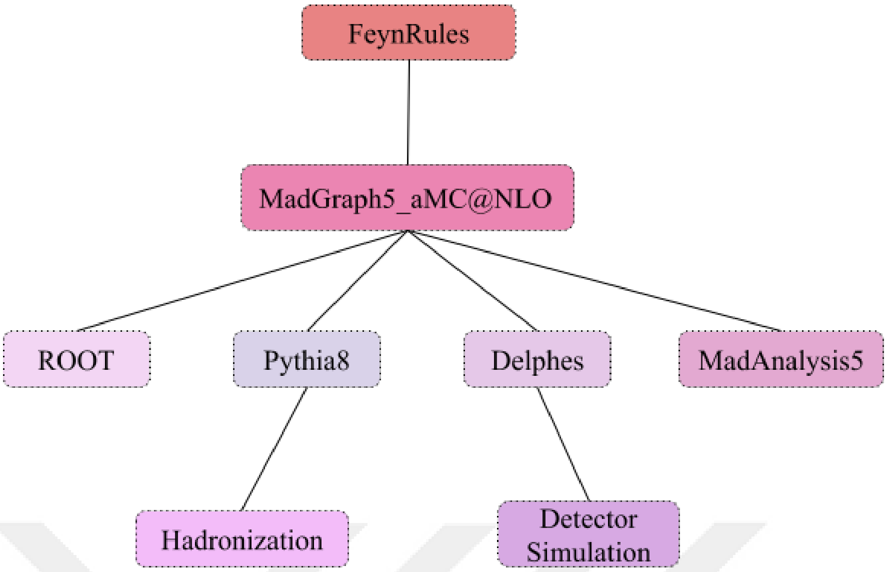

Figure 4.1. A software network for particle physics.

In Figure 4.1, a particle physics software network is visualized through a flow chart, depicting the interconnected processes and functionalities within the system. At first glance, this might seem like a complex puzzle to assemble, but in practice, the integration of these tools is quite straightforward. Notably, the MadGraph suite stands out for its ingenious design, streamlining the entire process by automating numerous essential steps. This automation not only enhances the robustness of our simulations but also guarantees a blend of efficiency and precision. It encompasses everything from the initial revelation and subsequent exploration of phenomena extending BSM of particle physics to the intricate task of quantifying their distinctive properties.

4.1 Event Generation

This section outlines the analysis specifics concerning the impact of dimension-8 operators on anomalous quartic gauge boson couplings through the tri-photon signal process, as applicable to upcoming hadron colliders.

Before delving into an extensive Monte Carlo simulation, it is beneficial to explore the impact of anomalous quartic couplings on the cross-section of tri-photon production for the formulation of an analysis strategy. Figure 4.2 presents

Feynman diagrams for γγγ production, featuring anomalous quartic gauge boson couplings f_{T8} and f_{T9}, as depicted in (a) γγγγ and (b) γγγZ, alongside (c) the Standard Model contribution.

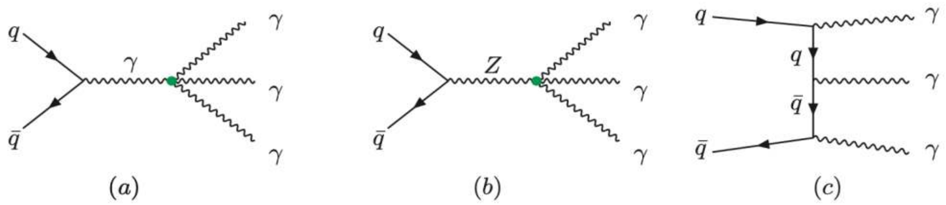

Figure 4.2. Contributions to γγγ Production at Hadron Colliders Illustrated by Feynman Diagrams: Anomalous Quartic Vector-Boson Interactions Explored in (a) and (b), Emphasizing Green Annotations in (c), Alongside the Standard Model's Role.

The total cross-section, arising from the summation of these three Feynman diagrams, takes the form of a quadratic function when only a single non-zero anomalous quartic coupling f_{Ti}/Λ^4 is active at a time, and can be expressed as follows:

$$\sigma_{tot} = \sigma_{SM} + \left(\frac{f_{Ti}}{\Lambda^4}\right)^2 \sigma_\gamma + \left(\frac{f_{Ti}}{\Lambda^4}\right)^2 \sigma_Z + \left(\frac{f_{Ti}}{\Lambda^4}\right)^2 \sigma_{\gamma Z} + \frac{f_{Ti}}{\Lambda^4}\sigma_{\gamma-SM} + \frac{f_{Ti}}{\Lambda^4}\sigma_{Z-SM} \quad (4.1)$$

where "σ_{SM}" represents the cross-section in the Standard Model for $\gamma\gamma\gamma$ production; The terms "σ_γ", "σ_Z", and "$\sigma_{\gamma Z}$" represent the pure anomalous cross-sections arising from the $\gamma\gamma\gamma\gamma$, $\gamma\gamma\gamma Z$ vertices, along with their interference, respectively; Notations $\sigma_{\gamma-SM}$ and σ_{Z-SM} signify the interference between Standard Model processes and the anomalous contribution to the $\gamma\gamma\gamma$ production.

Findings from Figure 4.3 strongly indicate that the cross section for the three-photon production is significantly more responsive to the f_{T8}/Λ^4 coupling compared to the f_{T9}/Λ^4 coupling at FCC-hh. Another noteworthy discovery from Figure 4.3 is that the primary factor influencing the change in the cross section concerning both f_{T8}/Λ^4 and f_{T9}/Λ^4 is attributed to the $\gamma\gamma\gamma\gamma$ vertex and its interaction with the Standard Model, rather than the $\gamma\gamma\gamma Z$ vertex. Figure 4.4 indicates that the cross sections of f_{T8}/Λ^4 and f_{T9}/Λ^4 couplings at a center-of-mass energy of $\sqrt{s} = 14\, TeV$ at HL-LHC.

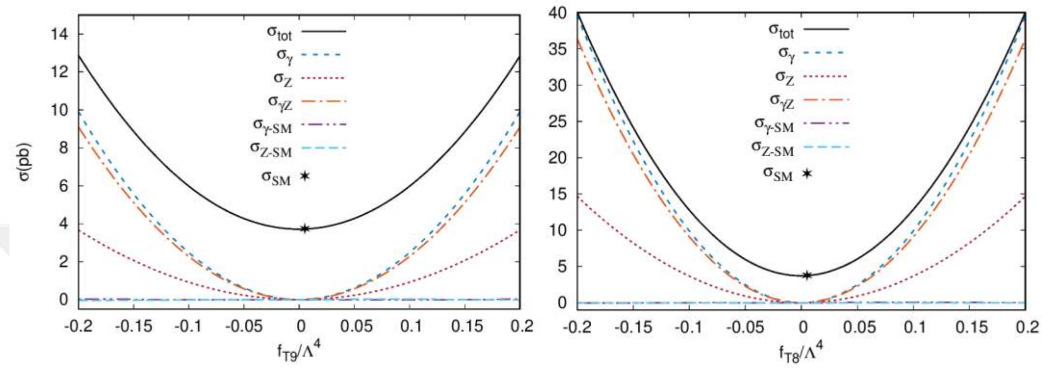

Figure 4.3. The cross section for the process pp → γγγ, depicted as a function of dimension-8 anomalous quartic gauge couplings f_{T9}/Λ^4 and f_{T8}/Λ^4 at a center-of-mass energy of $\sqrt{s} = 100\, TeV$, is influenced by the contributions of the γγγγ vertex (σ_{γ}), Zγγγ vertex (σ_{Z}), their interference ($\sigma_{\gamma Z}$), and the SM contributions ($\sigma_{\gamma-Z}$ and σ_{Z-SM}), all explored in the absence of applied form factors.

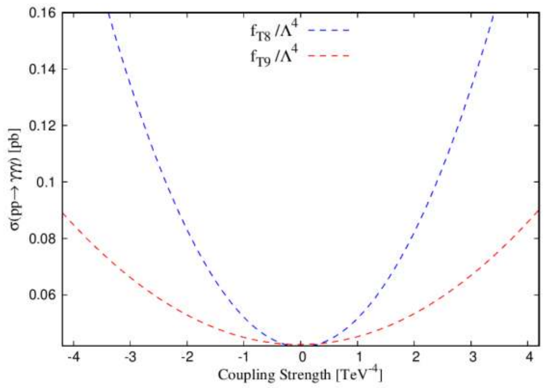

Figure 4.4. The cross section of the dimension-8 aQGCs, f_{T8}/Λ^4 and f_{T9}/Λ^4 at HL-LHC.

For a given initial and final state, all tree-level matrix elements are computed in the first step. This implies that all subprocesses are included in the final output. Individual subprocesses, such as QCD processes or anomalous couplings, can be switched off by setting the respective coupling constants to zero. Due to the confinement property inherent in QCD, it is impossible to directly observe individual quarks and gluons as isolated particles. Instead, when high-energy collisions produce partons, these partons emit additional partons, giving rise to cascades of hadrons known as "jets." The characteristics of the initial parton are intricately connected to the properties of the resulting jet. Therefore, jets serve as the bridge connecting the observable hadrons in the final state with critical information regarding PDFs and QCD parameters. Combining precise HL-LHC and FCC-hh data with state-of-the-art next-to-leading order (NLO) theoretical calculations for hadronic processes such as direct photon production and inclusive jet production greatly contributes to accurate PDF adaptations. To achieve this goal and perform cross-section calculations for the $pp \to \gamma\gamma\gamma$ process, the inclusion of effective vertices corresponding to $\gamma\gamma\gamma\gamma$ and $Z\gamma\gamma\gamma$ anomalous quartic gauge couplings within the Universal Feynrules Output (UFO) (39,40) framework is required. To simulate the behavior of a regular electromagnetic calorimeter and mitigate issues related to infrared divergences, we established a minimum requirement for the transverse momentum of photons in the final state at the generator level. Specifically, we set this requirement for event generation to be carried out with $p_T^\gamma > 15\,GeV$ for HL-LHC and $p_T^\gamma > 25\,GeV$ for FCC-hh, respectively. A total of 600.000 events were generated for each coupling with five different positive values of both f_{T8}/Λ^4 and f_{T9}/Λ^4, both for the signal and all relevant background processes, using the MadGraph5_aMC@NLO (41) framework with the NNPDF23LO PDF set (42). Events are generated with weights corresponding to an effective luminosity of 30 ab^{-1} for FCC-hh and 3 ab^{-1} for HL-LHC. While our analysis primarily focuses on the identification of isolated three photons in the final state, the signal process under consideration faces challenges from background sources, particularly high-p_T jets. These jets, even stringent identification and isolation criteria, can be misidentified as isolated photons, introducing complexities to the analysis. Therefore, in the analysis of the $pp \to \gamma\gamma\gamma$ signal prcess, relevant background processes such as multi-jet photons (jjj), photon + jet (γjj), and diphoton-jet ($\gamma\gamma j$) backgrounds are included in addition to the SM background, which shares the same final state as the signal process.

Table 4.1 provides a detailed comparative analysis of the total cross-sections for various background processes. These processes include the production of $\gamma\gamma\gamma$, $\gamma\gamma j$, γjj, and jjj at both the HL- LHC with a center-of-mass energy of $\sqrt{s} = 14\ TeV$ and the FCC-hh proton-proton collision with $\sqrt{s} = 100\ TeV$.

Table 4.1. The total cross section (pb) for the production of $\gamma\gamma\gamma$, $\gamma\gamma$j, γjj, and jjj processes at $\sqrt{s} = 14\ TeV$ (with p_T^{γ} > 15 GeV) and $\sqrt{s} = 100\ TeV$ (p_T^{γ} > 25 GeV).

	Cross sections (pb)	
Processes	$\sqrt{s} = 14\ TeV$	$\sqrt{s} = 100\ TeV$
$pp \to \gamma\gamma\gamma$	4.349×10^{-2}	5.741×10^{-2}
$pp \to \gamma\gamma j$	5.405×10^{-2}	1.464×10^{-2}
$pp \to \gamma jj$	5.148×10^{-2}	2.181×10^{-2}
$pp \to jjj$	8.022×10^{-2}	1.239×10^{-2}

Subsequently, in all cases, the events generated at the parton level undergo parton showering and hadronization processes using Pythia 8.20 (43), as mentioned earlier. The signal and background samples are scaled using the most precise cross-section calculations, which align with NLO accuracy. Following the hadronization process, the inclusion of realistic detector effects is achieved with the Delphes 3.4.2 (44) version. We utilized specially designed enhanced configuration cards, namely delphes_card_HLLHC_aqgc.tcl and FCC-hh.tcl, tailored for HL-LHC and FCC-hh, respectively. These detector configuration files are where the detector response, expressed through resolution functions and efficiencies, is characterized. The reconstruction of jets involves the utilization of clustered energy deposits, implemented using the FastJet 3.3.2 (45) library, and applying the anti-kt algorithm (46).

In this process, a cone radius is defined as $\Delta R = 0.2$, and a minimum transverse momentum requirement of $p_T^j > 20\ GeV$ is imposed for both detectors. The likelihood of mistakenly identifying a jet as a photon depends on the interaction dynamics between the jets and the detector. At this time, the likelihood of mistakenly reconstructing a high-energy scattering jet as an isolated photon is extremely low. This is mainly because the existing calorimeters in the LHC detectors offer outstanding angular precision. Predictions for future hadron-hadron colliders, equipped with advanced detector setups, suggest that these detectors will have 2-4 times finer granularity compared to the current LHC detectors. To account for this, we have incorporated a constant fake rate of 10^{-3} for jets in the γγj, γjj, and jjj background processes.

4.2 TMVA Methods

TMVA, short for the Toolkit for Multivariate Analysis, seamlessly integrates with the ROOT framework, creating a unified environment for conducting advanced multivariate classification tasks, all with the added capability of parallel execution. It is tailored to support the classification of events typically categorized into two classes, often referred to as signal and background. TMVA stands out as a versatile software package, delivering object-oriented implementations in C++/ROOT for a diverse collection of discrimination techniques. Beyond its classifiers, TMVA offers a valuable set of auxiliary tools, such as parameter fitting and variable transformations. This comprehensive package includes a wide range of functionalities, covering everything from training and testing to performance evaluation algorithms, along with an assortment of visualization scripts that prove invaluable for data analysis and model assessment.

In the context of TMVA, a Boosted Decision Tree (BDT) (47-50) is a machine learning algorithm used for classification and regression tasks. In the realm of particle physics, BDTs are commonly harnessed for the critical task of identifying and differentiating various particle types, such as electrons, muons, and hadrons. They leverage the data collected by particle detectors to make precise particle classification possible. A BDT is an ensemble learning method that combines multiple decision trees to create a more powerful and accurate predictive model. The key idea behind boosting is to train a sequence of decision trees, where each subsequent tree focuses on the errors made by the previous ones. This allows it to iteratively improve its performance and make better predictions. Boosted decision trees can be seen as an extension or enhancement of a single decision tree. In the TMVA framework, the conventional AdaptiveBoost (AdaBoost) algorithm (51), specifically optimized for classification problems, is available. AdaBoost is an ensemble learning algorithm that combines weak learners trained sequentially to form a strong learner. This algorithm determines the boost weight for constructing the next tree based on the count of misclassified training events in the previously trained tree and assigns higher weights to these events. Specifically designed for high-energy physics studies, open-source libraries such as AdaBoost can be harnessed to effectively implement boosted decision trees. At each "node" of the decision tree, specific cuts are strategically applied to these variables, aiming to maximize the separation between background and signal. Strategic placement of cuts for each variable optimizes the discrimination between background and signal events. Every event traverses the decision tree, navigating through a sequence of nodes and selecting one of two branches at each node based on the value of the associated variable. As events undergo multiple cuts, they ultimately reach a "leaf." After numerous events have passed through this decision tree, multiple events accumulate in each leaf, contributing to the classification of background and signal events. Assigning a score to each leaf based on the ratio of background events to signal events captured helps in further categorization. Leaves with a score below 1, indicating a higher prevalence of background events, are labeled as background, while leaves with a score exceeding 1 are identified as signal. This detailed procedure is visually elucidated in Figure 4.5.

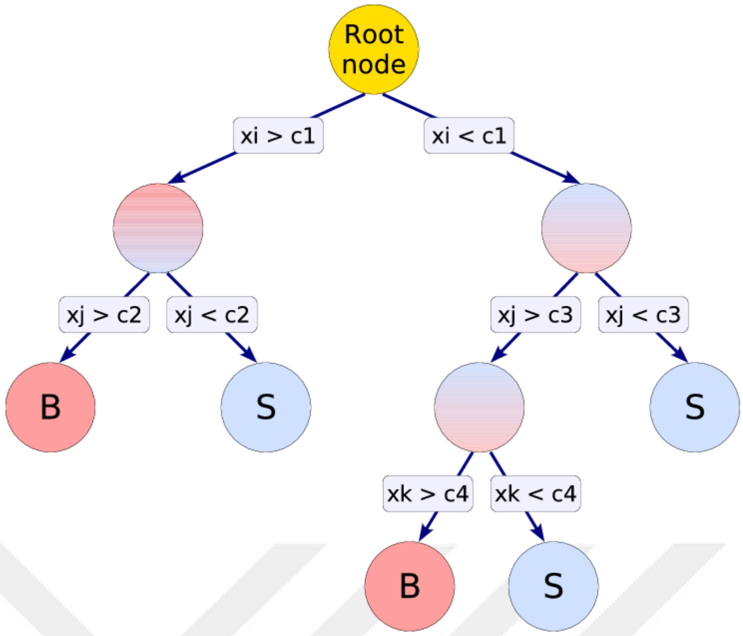

Figure 4.5. Illustration of a Decision Tree Structure (52).

As mentioned earlier, to distinguish between background and signal in particle physics analyses, Monte Carlo samples are required for both. After the establishment of a well-trained decision tree, its effectiveness is assessed by subjecting additional Monte Carlo-generated events to the same cutting process. These samples not only form the basis for training the analysis but also play a vital role in validating the training process. Events directed to a "signal" leaf are categorized as signal events, while those directed to a "background" leaf are identified as background events. Decision trees play a crucial role in this context, effectively distinguishing between background and signal events using selected variables from the analysis.

By harnessing these methodologies, we can gain a comprehensive understanding of our BDT model's efficiency and robustness. Cross-validation ensures that the model's performance is stable across various data subsets, while Receiver Operating Curve (ROC) provides nuanced insights into discriminatory power and overall effectiveness in distinguishing between signal and background events. This multifaceted evaluation process empowers us to fine-tune our model and make well-informed decisions about its suitability for the given task.

The event selection process commences by requiring a minimum of three photons in both the signal and all relevant background processes. F ollowing this, generator-level cuts are carefully implemented on the final state particles, ensuring the quality and reliability of the selected events. To effectively capture the kinematic distinctions between signal and background processes, a BDT undergoes training, incorporating a diverse set of kinematic information detailed in Table 4.2.

Table 4.2. The compilation of chosen kinematic and reconstructed variables intended for BDT (53).

Variable	Definition
$p_T^{\gamma_1}$	Transverse momentum of the leading photon
$p_T^{\gamma_2}$	Transverse momentum of the second-highest-p_T photon
$p_T^{\gamma_3}$	Transverse momentum of the third-highest-p_T photon
η^{γ_1}	Pseudo-rapidity of the leading photon
η^{γ_2}	Pseudo-rapidity of the second-highest-p_T photon
η^{γ_3}	Pseudo-rapidity of the third-highest-p_T photon
$\Delta\|\phi^{\gamma_1\gamma_2}\|$	Difference in azimuthal angle between the leading and second-highest-p_T photons
$\Delta\|\phi^{\gamma_1\gamma_3}\|$	Difference in azimuthal angle between leading and the third-highest-p_T photon
$\Delta\|\phi^{\gamma_2\gamma_3}\|$	Difference in azimuthal angle between second-highest-p_T photon and the third-highest-p_T photon
$\Delta\|\eta^{\gamma_1\gamma_2}\|$	Difference in pseudo-rapidity between the leading and the second-highest-p_T photons
$\Delta\|\eta^{\gamma_1\gamma_3}\|$	Difference in pseudo-rapidity between the leading and the third-highest-p_T photon
$\Delta\|\eta^{\gamma_2\gamma_3}\|$	Difference in pseudo-rapidity between the second-highest-p_T and the third-highest-p_T photon
$\Delta R(\gamma_1, \gamma_2)$	Distance between leading photon and sub-leading photon in η-ϕ plane
$\Delta R(\gamma_2, \gamma_3)$	Distance between sub-leading photon and third photon in η-ϕ plane
$\Delta R(\gamma_1, \gamma_3)$	Distance between leading photon and third photon in η-ϕ plane
N_j	Number of jets in the event
$m_{\gamma_1\gamma_2\gamma_3}$	Invariant mass of reconstructed three photon system

The input variables for the multivariate Boosted Decision Tree (BDT) discriminant include the transverse momentum and pseudo-rapidity of the top three photons (γ_1, γ_2, and γ_3), ranked by their p_T. These variables help capture the energy and direction of the individual photons.

Moreover, the discriminant takes into account variations in the azimuthal angle and pseudo-rapidity among photon pairs, the spatial disjunction between photon pairs in the η-φ plane, the invariant mass of the tri-photon system ($m_{\gamma_1\gamma_2\gamma_3}$), and the count of jets in the final state. Differences in azimuthal angle (Δϕ) and pseudo-rapidity (Δη) among photon pairs can reveal angular correlations and separation between the photons. Quantifying the geometric arrangement of photons in an event, the spatial separation between photon pairs in the η-φ plane serves to elucidate their distribution. As we aim to robustly differentiate our signal from Standard Model backgrounds, particularly those involving jets in the final state, the incorporation of the jet count becomes a crucial input variable in the BDT. While the number of jets holds importance in effectively discerning the signal from Standard Model backgrounds featuring jets in the final state, the specific kinematic properties of the jets are intentionally omitted from consideration in this analysis.

Within the array of variables outlined in Table 4.2 for the multivariate BDT discriminant, the chosen target variable for BDT analysis is the invariant mass of the tri-photon system. This variable distinctly characterizes the total energy and momentum of the three photons. By including these input variables in the BDT, the algorithm can effectively discriminate between signal and background events based on their kinematic features. The BDT's ability to learn and model the relationships between these variables allows it to make informed decisions about the event's classification, making it a powerful tool for event selection in the analysis.

For optimal results, meticulous adjustments to parameters, including the number of trees, tree depth, and learning rate, are imperative. In this context, our multivariate analysis harnesses the BDT machine learning technique, employing carefully chosen hyperparameters.

We utilize a total of 850 decision trees in our BDT model. This allows us to capture complex relationships in the data. To limit the depth of individual trees, prevent overfitting, and ensure a more generalizable model, the maximum depth of each decision tree is set to 3. We require a minimum of 2.5 events at each final leaf node. This constraint helps maintain the quality of the splits and prevents overly fine-grained leaves that could lead to overfitting. During the training process, we performed 20 iterations to find the best split for the decision trees. This helps optimize the quality of the splits and improve the overall model performance. Signal events from the training sample might be misclassified as background events due to the trade-off in learning rates—opting for a higher learning rate could accelerate convergence but at the cost of stability, whereas a lower learning rate offers more stable convergence. Therefore, the learning rate is fixed at 0.5, governing the step size in the optimization process. Consequently, half of the combined data is dedicated to the training phase, while the remaining 50% is set aside for testing purposes. This combination of hyperparameters is used to train and optimize the BDT model for our analysis. Adjusting these parameters can impact the performance and generalization of the model, so it's essential to fine-tune them to achieve the best results for a particular application. It is possible to train TMVA using any selection cuts that are desired. In the BDT analysis process, The invariant mass of the three photons is applied to signal and background events to cut individually ($m_{\gamma_1\gamma_2\gamma_3} < x$) and was selected based on different aQGC values for f_{T8}/Λ^4 and f_{T9}/Λ^4 couplings. Here, the cut x value is determined depending on the unitary violation bond calculation for each coupling.

After completing the BDT analysis, TMVA provides BDT signal efficiency values to assist in determining the optimal cut. In the process of determining an optimal cut, we consider a 70% signal efficiency in the reconstructed BDT distributions. As each signal is individually trained in the BDT analysis, adapted to different aQGC values for f_{T8}/Λ^4 and f_{T9}/Λ^4 couplings, distinct BDT scores are derived for each signal and all relevant Standard Model backgrounds. Leveraging the obtained BDT scores, we subsequently apply them to both signal and all relevant background processes to extract the invariant mass distributions of three-photon systems.

ROC curves provide a visual representation of the balance between the true positive rate and false positive rate across various discrimination thresholds. TMVA facilitates the creation of these curves, offering a comprehensive view of how effectively the BDT model distinguishes signal from background events. As clearly seen from the Figure 4.6, the BDT algorithm effectively distinguishes the signal from the backgrounds. The plot located at the top left in Figure 4.6 represents the BDT response for the signal with f_{T8}/Λ^4 = 0.03 TeV^{-4} alongside all relevant backgrounds in the trained samples at FCC-hh. Conversely, the plot in the top-right, known as the ROC curve, graphically represents the trade-off between signal efficiency and background rejection. The clear depiction in Figure 4.6 emphasizes the robust performance of the BDT algorithm.

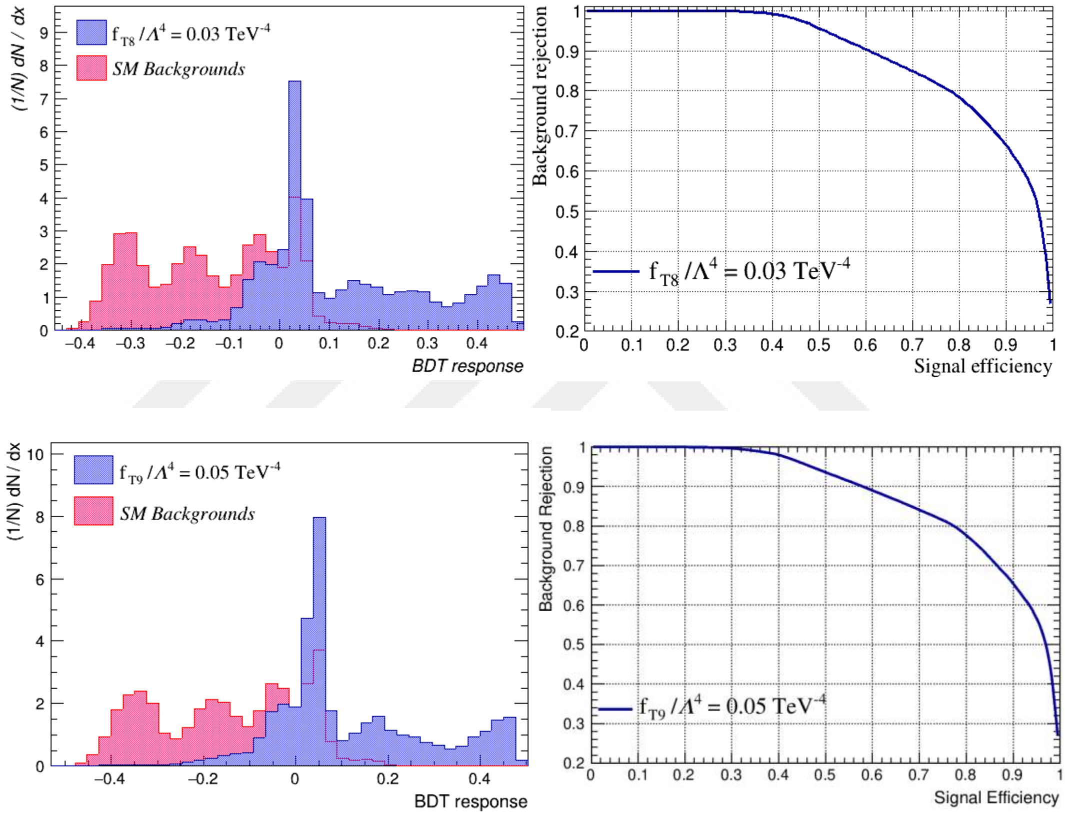

Figure 4.6. The BDT Response Distribution on the left and the ROC Curve on the right, depicting signal (f_{T8}/Λ^4 = 0.03 TeV^{-4} and f_{T9}/Λ^4 = 0.05 TeV^{-4}) and all relevant backgrounds. Achieved outcomes at FCC-hh with integrated luminosity L_{int} = 30 ab^{-1}.

The two plots at the bottom of Figure 4.6 depict the BDT response and ROC curve for the signal with f_{T9}/Λ^4 = 0.05 TeV^{-4} at FCC-hh, alongside all relevant background scenarios. As evident from this illustration, the BDT performs exceptionally well, effectively distinguishing the signal from the backgrounds.

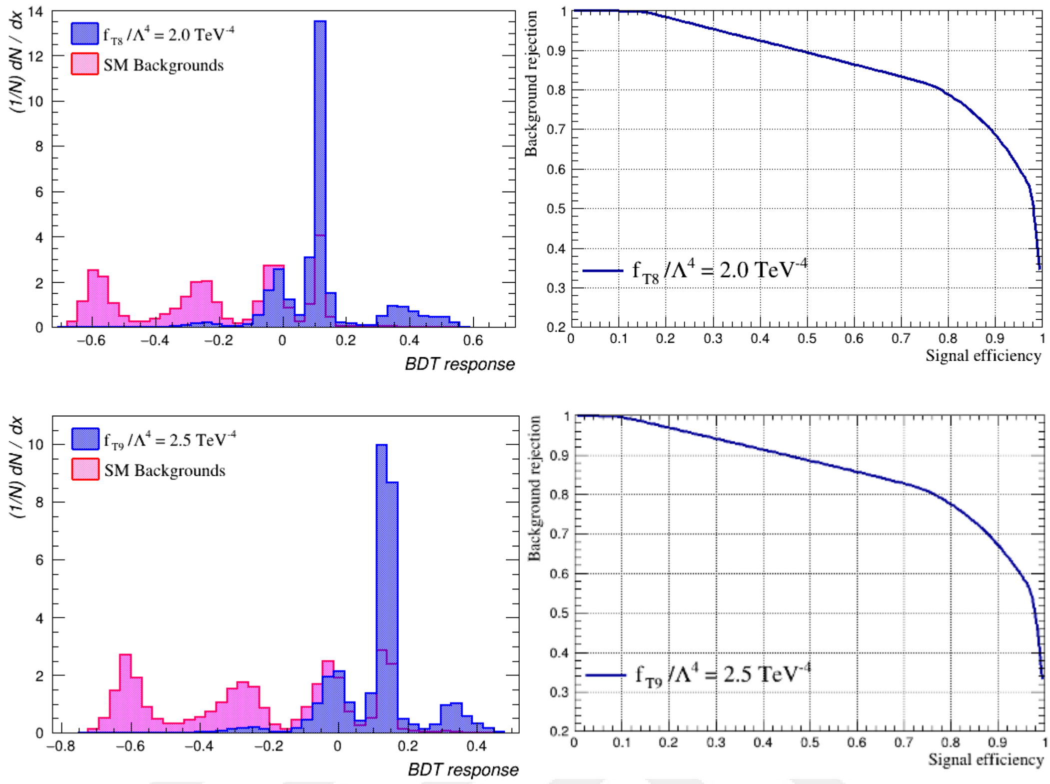

Figure 4.7. The BDT Response Distribution (left) and ROC Curve (right) for signal ($f_{T8}/\Lambda^4 = 2.0\ TeV^{-4}$ and $f_{T9}/\Lambda^4 = 2.5\ TeV^{-4}$) and backgrounds. Achieved outcomes at HL-LHC with integrated luminosity $L_{int} = 3\ ab^{-1}$.

In Figure 4.7, the upper-left plot visually captures the BDT response for the signal with $f_{T8}/\Lambda^4 = 2.0\ TeV^{-4}$ in the trained samples at HL-LHC, accompanied by all relevant background scenarios. Conversely, the upper-right plot, designated as the ROC curve, provides a graphical representation of the delicate balance between signal efficiency and background rejection. The distinct presentation in Figure 4.7 accentuates the strong and reliable performance of the BDT algorithm.

The two charts at the bottom of Figure 4.7 show how well the BDT and the ROC curve perform for the signal with $f_{T9}/\Lambda^4 = 2.5\ TeV^{-4}$ at HL-LHC, compared to all the relevant background situations. Consequently, one can establish the optimal cut on reconstructed BDT distributions by taking into account signal efficiency.

Effective operators result in a breakdown of unitarity at high energy levels, prompting the need to restrict the parameterization of deviations from SM predictions to energy regimes devoid of such violations. In this analysis, a widely used technique referred to as the clipping method (26,54) is employed to mitigate unitarity violations. The clipping method involves the suppression of any contribution from EFT beyond a specified energy scale denoted as ΛFF. This approach ensures that calculations and predictions remain reliable within the chosen energy boundaries, preserving the integrity of the theoretical framework in the absence of unitarity issues. The determination of the appropriate energy scale, ΛFF, is a critical step, and its calculation involves considering factors specific to the effective field theory, thus providing a robust means of addressing unitarity concerns in high-energy scenarios

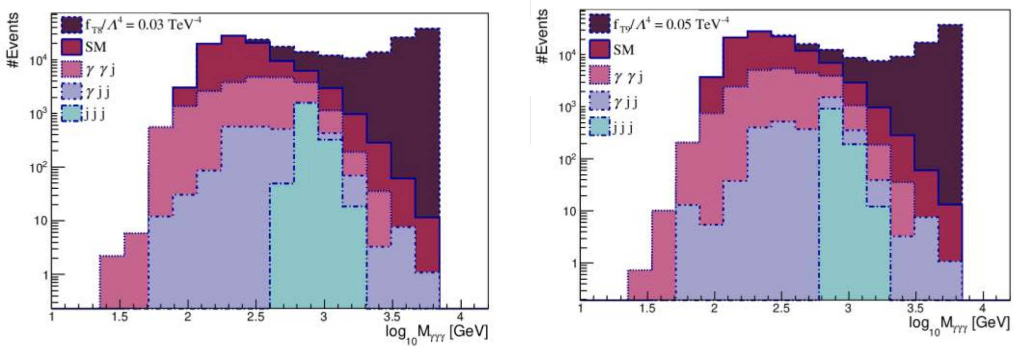

Figure 4.8. The normalized distribution showcases the invariant mass of the reconstructed tri-photon system for the signal and all relevant background processes, considering aQGC values f_{T8}/Λ^4 = 0.03 TeV^{-4} and f_{T9}/Λ^4 = 0.05 TeV^{-4} at FCC-hh, with an integrated luminosity of L_{int} = 30 ab^{-1}.

The determination of the energy scale, ΛFF, for each anomalous QGC parameter involves calculations using VBFNLO, incorporating relevant aQGC convention factors. Subsequently, the energy threshold for clipping is applied to the invariant mass of $m_{\gamma_1\gamma_2\gamma_3}$ for each aQGC parameter. In Figure 4.8, the left side presents the normalized invariant mass distribution of the tri-photon system for the signal, featuring benchmark points f_{T8}/Λ^4 = 0.03 TeV^{-4} and f_{T9}/Λ^4 = 0.05

TeV^{-4}. On the right side, relevant backgrounds are depicted. These figures, individually calculated for each coupling (f_{T8}/Λ^4 or f_{T9}/Λ^4) from its SM value, are normalized to the cross-section of each process multiplied by the integrated luminosity, $L_{int} = 30\ ab^{-1}$.

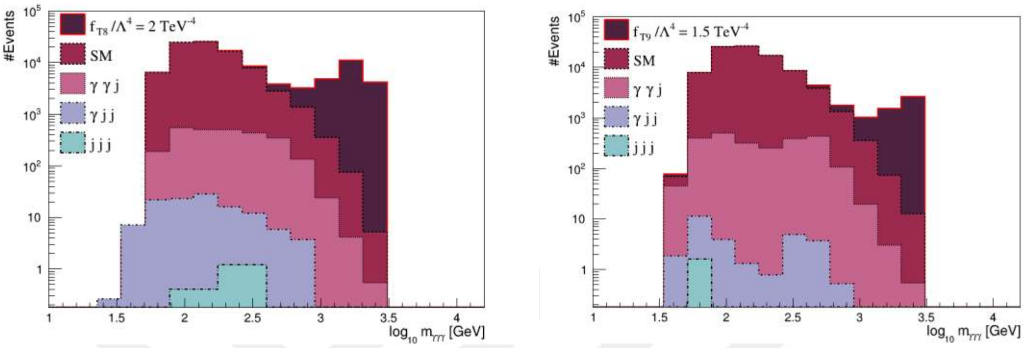

Figure 4.9. The normalized distribution showcases the invariant mass of the reconstructed tri-photon system for the signal and all relevant background processes, considering aQGC values $f_{T8}/\Lambda^4 = 2.0\ TeV^{-4}$ and $f_{T9}/\Lambda^4 = 1.5\ TeV^{-4}$ at HL-LHC, with an integrated luminosity of $L_{int} = 3\ ab^{-1}$.

Figure 4.9, on the other hand, illustrates the normalized invariant mass distribution of the tri-photon system, highlighting the signals $f_{T8}/\Lambda^4 = 2.0\ TeV^{-4}$ and $f_{T9}/\Lambda^4 = 1.5\ TeV^{-4}$. Similar to Figure 4.8, these visualizations are normalized to the cross-section of each process, multiplied by the integrated luminosity $L_{int} = 3\ ab^{-1}$, and are performed individually for each coupling of f_{T8}/Λ^4 and of f_{T9}/Λ^4 with respect to its SM value.

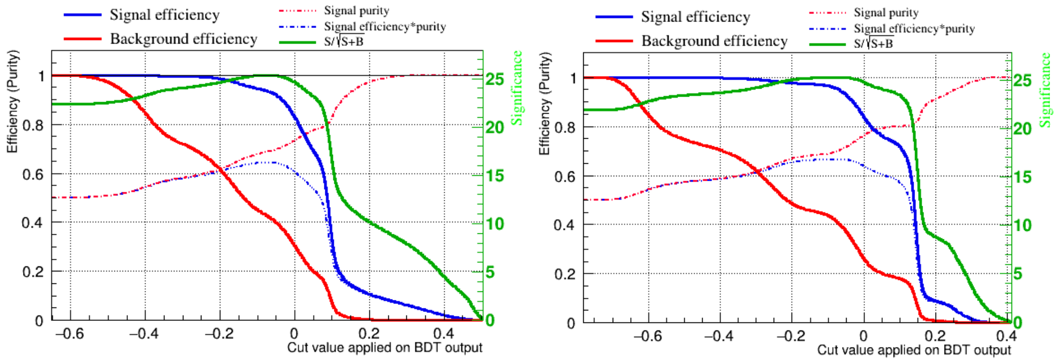

Figure 4.10. The BDT Classifier Cut Efficiencies is provided for the $pp \rightarrow \gamma\gamma\gamma$ with aQGC values of with $f_{T9}/\Lambda^4 = 0.03\ TeV^{-4}$ at FCC-hh and with $f_{T8}/\Lambda^4 = 1.0\ TeV^{-4}$ at HL-LHC.

BDT classifier cut efficiencies refer to the accuracy in classifying examples that fall below or above a specific threshold value. These efficiencies are important metrics for assessing the classifier's ability to distinguish between different categories based on the chosen cut value. The Figure 4.10 shows classifier cut efficiencies for 1000 signal and 1000 background events the maximum $S/\sqrt{S+B}$ is 25.3530 (25.79) when cutting at -0.0676 (-0.07) for FCC-hh (HL-LHC).

4.3 Limit on Anomalous Quartic Gauge Couplings

Anomalos quartic gauge couplings are described through a parametrization based on a dimension-8 effective field theory. The SM Lagrangian is extended in the EFT to include terms with dimensions greater than four, without distorting its meaning. Eighteen operators with a dimension of 8 contribute to the $\gamma\gamma\gamma\gamma$ and $\gamma\gamma\gamma Z$ vertices. Our study primarily centers on couplings involving products of electroweak field strength tensors, specifically those constrained by this analysis: f_{T8} and f_{T9}. Anomalus quartic gauge couplings amplify the generation of signal events at elevated momentum scales.

To compute the median expected statistical significance for the discovery (SS_{disc}) and exclusion (SS_{excl}) of the f_{T8}/Λ^4 and f_{T9}/Λ^4 couplings, as denoted in reference (55), we utilize the formulations presented in the specified source.

$$SS_{disc} = \sqrt{2\left[(S+B)\ln\left(\frac{(S+B)(1+\delta^2 B)}{B+\delta^2 B(S+B)}\right) - \frac{1}{\delta^2} ln\left(1+\delta^2 \frac{S}{1+\delta^2 B}\right)\right]} \tag{4.1}$$

$$SS_{excl} = \sqrt{2\left[S - Bln\left(\frac{B+S+x}{2B}\right) - \frac{1}{\delta^2} ln\left(\frac{B-S+x}{2B}\right)\right] - (B+S-x)\left(1+\frac{1}{\delta^2 B}\right)} \tag{4.2}$$

Where $x = \sqrt{(S+B)^2 - 4\delta^2 SB^2/(1+\delta^2 B)}$;

S and B represent the event counts obtained by integrating the normalized invariant mass distributions of the tri-photon system for the signal and the total Standard Model background, respectively, with δ denoting the systematic uncertainty. As the systematic uncertainty δ approaches zero, these expressions can be simplified to:

$$SS_{disc} = \sqrt{2\left[(S+B)\ln\left(1+\frac{S}{B}\right) - S\right]} \tag{4.3}$$

$$SS_{excl} = \sqrt{2[S + Bln(1+S/B)]} \tag{4.4}$$

Regions where SS_{disc} exceeds 5σ and 3σ are classified as discoverable areas, while regions with SS_{excl} exceeding 1.645 are identified as areas that can be excluded at 95% C.L. Figure 4.11 illustrates SS_{disc} and SS_{excl} as functions of aQGCs f_{T8}/Λ^4 (on the left panel) and f_{T9}/Λ^4 couplings for $L_{int} = 30\ ab^{-1}$ without (on the first row) and with δ set to 10% (on the second row) systematic uncertainty. In this visual representation, each figure explores the variation of only one coupling at a time from its SM value. The limits on dimension-8 aQGCs f_{T8}/Λ^4 and f_{T9}/Λ^4 can be deduced from the intersection points of curves with horizontal red and blue lines, indicating 3σ and 5σ significance levels in the left panel, and with a red line denoting the 95% C.L. in the right panel. The limits we derived for 3σ, 5σ, and 95% C.L., both without and with a δ set to 10% systematic uncertainties on dimensioneight aQGCs f_{T8}/Λ^4 and f_{T9}/Λ^4, are documented in Tables 4.3 and 4.4. These limits were obtained with an integrated luminosity $L_{int} = 30\ ab^{-1}$.

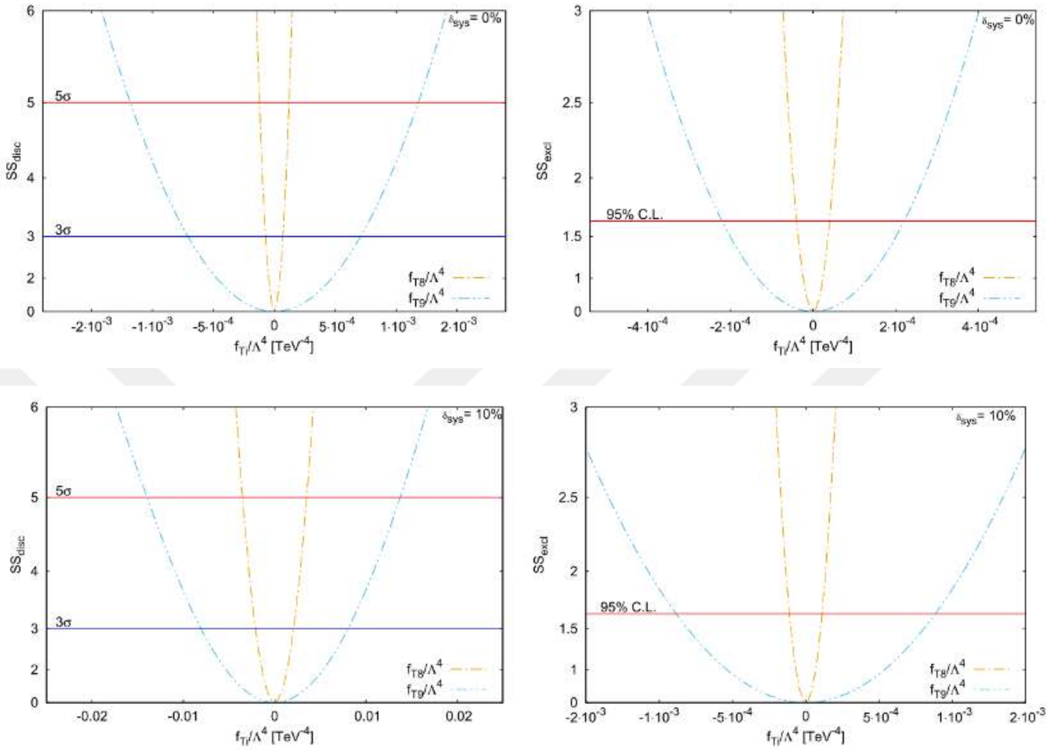

Figure 4.11. The SS_{disc} and SS_{excl} at $\delta \to 0\%$ and $\delta \to 10\%$ couplings for f_{T8}/Λ^4 and f_{T9}/Λ^4 at FCC-hh.

The ATLAS collaboration recently disclosed the most stringent constraints on aQGCs f_{T8}/Λ^4 and f_{T9}/Λ^4. These limits are based on the measured cross section of electroweak production of $Z(\nu\bar{\nu})\gamma$ in association with two jets, and they incorporated the application of the clipping technique. At a 95% C.L., the current limits, derived from an integrated luminosity of 139 fb^{-1} at $\sqrt{s} = 13$ TeV, stand at $[-5.2;\ 5.2] \times 10^{-1}$ (with ΛFF=1.7 TeV) for f_{T8}/Λ^4 and $[-7.9;\ 7.9] \times 10^{-1}$ (with ΛFF=1.9 TeV) for f_{T9}/Λ^4, respectively.

As indicated in Table 4.3 (4.4), our constraints on aQGCs f_{T8}/Λ^4 (f_{T9}/Λ^4) without systematic errors at 5σ and 95% C.L. are [-7.31; 7.31] × 10^{-5} ([-4.59; 4.59] × 10^{-4}), and [-4.01; 4.01] × 10^{-5} ([-2.20; 2.20] × 10^{-4}), respectively. When comparing our limits with those recently reported by the ATLAS collaboration, our results are more than three orders of magnitude more precise. Even when considering a 10% systematic error, our outcomes at 5σ and 95% C.L. still surpass by two orders of magnitude.

Table 4.3. Constraints on f_{T8}/Λ^4 $[TeV^{-4}]$ at 3σ, 5σ, and 95% C.L., both without and with δ set to 10% systematic uncertainties, for an integrated luminosity of L_{int} = 30 ab^{-1} at FCC-hh.

δ_{sys}	3σ	5σ	95% C.L.
0	[-7.31;7.31]× 10^{-5}	[-1.21;1.21] × 10^{-4}	[-4.01;4.01] × 10^{-5}
10%	[-2.98;2.98] × 10^{-3}	[-3.51;3.51] × 10^{-3}	[-1.11;1.11] × 10^{-4}

Table 4.4. Constraints on f_{T9}/Λ^4 $[TeV^{-4}]$ at 3σ, 5σ, and 95% C.L., both without and with δ set to 10% systematic uncertainties, for an integrated luminosity of L_{int} = 30 ab^{-1} at FCC-hh.

δ_{sys}	3σ	5σ	95% C.L.
0	[-4.59;4.59]× 10^{-4}	[-7.65;7.65] × 10^{-4}	[-2.20;2.20] × 10^{-4}
10%	[-8.06;8.06] × 10^{-3}	[-4.43;4.43] × 10^{-2}	[-8.84;8.84] × 10^{-4}

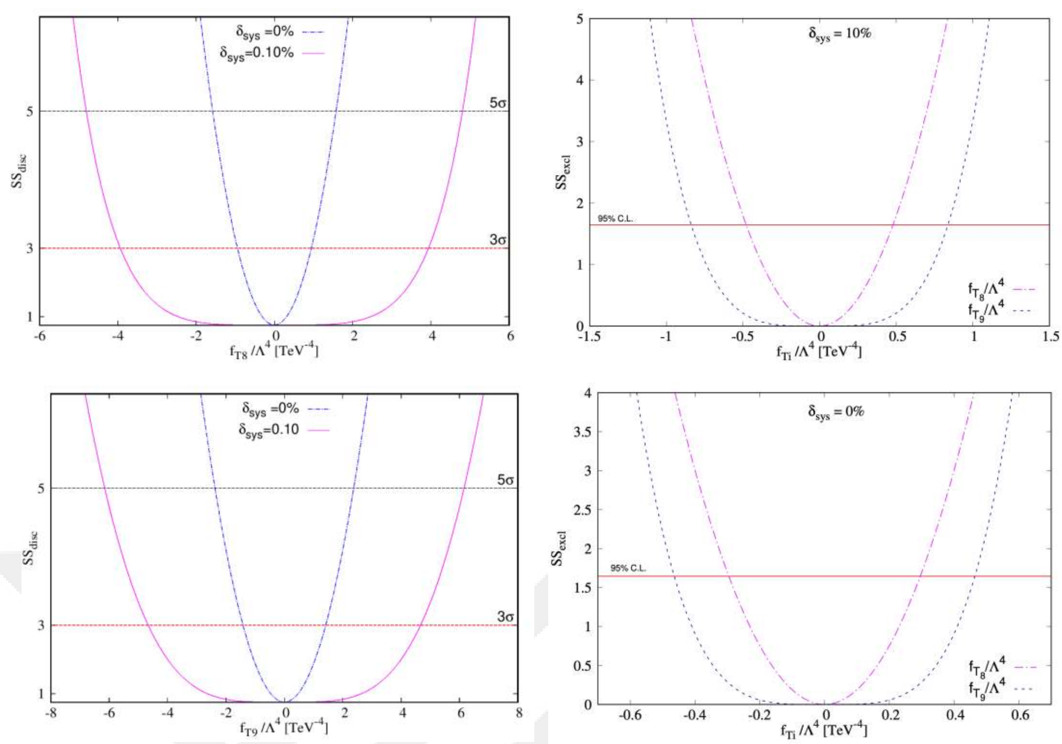

Figure 4.12. The SS_{disc} and SS_{excl} at $\delta \rightarrow 0\%$ and $\delta \rightarrow 10\%$ couplings for f_{T8}/Λ^4 and f_{T9}/Λ^4 at HL-LHC.

Figure 4.12 illustrates the SS_{disc} and SS_{excl} as functions of aQGCs f_{T8}/Λ^4 (on the left panel) and f_{T9}/Λ^4 couplings for $L_{int} = 3\ ab^{-1}$ without (on the first row) and with δ set to 10% (on the second row) systematic uncertainty for HL-LHC. In this visual representation, each figure explores the variation of only one coupling at a time from its SM value. The limits on dimension-8 aQGCs f_{T8}/Λ^4 and f_{T9}/Λ^4 can be deduced from the intersection points of curves with horizontal red and blue lines, indicating 3σ and 5σ significance levels in the left panel, and with a red line denoting the 95% C.L. in the right panel. The limits we derived for 3σ, 5σ, and 95% C.L., both with (a δ set to 10%) and without systematic uncertainties on dimension-8 aQGCs f_{T8}/Λ^4 and f_{T9}/Λ^4, are documented in Tables 4.5 and 4.6. These limits were obtained with an integrated luminosity $L_{int} = 3$ ab^{-1}. As seen in the Table 4.5 (4.6), the constraints on aQGCs f_{T8}/Λ^4 (f_{T9}/Λ^4) without systematic errors at 5σ and 95% C.L. are [-1.57;1.57] × 10^1 ([-2.95;2.95] × 10^{-1}), and [-9.00;9.00] × 10^1 ([-4.60;4.60] × 10^{-1}) at HL-LHC, respectively.

Table 4.5. Constraints on f_{T8}/Λ^4 $[TeV^{-4}]$ at 3σ, 5σ, and 95% C.L., considering both scenarios with and without δ, set to 10% systematic uncertainties, based on an integrated luminosity of $L_{int} = 3\ ab^{-1}$ at the HL-LHC.

δ_{sys}	3σ	5σ	95% C.L.
0	[-9.41;9.41]$\times 10^{-1}$	[-1.57;1.57] $\times 10^{0}$	[-2.95;2.95] $\times 10^{-1}$
10%	[-3.93;3.93] $\times 10^{0}$	[-4.81;4.81] $\times 10^{0}$	[-4.80;4.80] $\times 10^{-1}$

Table 4.6. Constraints on f_{T9}/Λ^4 $[TeV^{-4}]$ at 3σ, 5σ, and 95% C.L., considering both scenarios with and without δ, set to 10% systematic uncertainties, based on an integrated luminosity of $L_{int} = 3\ ab^{-1}$ at the HL-LHC.

δ_{sys}	3σ	5σ	95% C.L.
0	[-6.93;6.93]$\times 10^{-1}$	[-9.00;9.00] $\times 10^{-1}$	[-4.60;4.60] $\times 10^{-1}$
10%	[-4.54;4.54] $\times 10^{0}$	[-6.00;6.00] $\times 10^{0}$	[-8.37;8.37] $\times 10^{-1}$

5. CONCLUSION

The remarkable capabilities of the future hadron colliders, including its high center-of-mass energy and luminosity, coupled with advancements in detector technologies, provide an unprecedented opportunity to probe physics beyond the SM. Exploring tri-photon production within hadron colliders emerges as an optimal way for detecting deviations from the SM. This process, while infrequent within the SM, exclusively incorporates pure electroweak interaction contributions at the tree level, making it an ideal platform for probing physics beyond the SM.

This thesis delves into the investigation of aQGCs, focusing on tri-photon production at future hadron colliders, namely FCC-hh and HL-LHC. Under the assumptions of a 50 TeV proton beam energy and 30 ab^{-1} integrated luminosity for FCC-hh, and a 7 TeV proton beam energy and 3 ab^{-1} integrated luminosity for HL-LHC, this study focuses on a series of aQGCs, particularly those associated with dimension-8 EFT operators contributing to quartic vertices such as $\gamma\gamma\gamma Z$ and $\gamma\gamma\gamma\gamma$. Because of the increased sensitivity of aQGCs associated with $\mathcal{O}_{T,8}$ and $\mathcal{O}_{T,9}$ operators to tri-photon production, the cross section has been computed by considering both the pure contribution of aQGCs and the interference between the SM process and aQGCs f_{T8}/Λ^4 and f_{T9}/Λ^4 in $pp \rightarrow \gamma\gamma\gamma$ production. The signal, characterized by a minimum of three photons in the final state, was considered additionally along with three dominant background processes intricately tied to our signal, all meticulously simulated at the detector level. An additional layer of our investigation involved probing potential violations stemming from unitarity in the context of the dimension-8 aQGCs that captivated our interest.

To explore the potential enhancement of sensitivity for f_{T8}/Λ^4 and f_{T9}/Λ^4, a multivariate analysis was conducted. This analysis incorporated 17 kinematic variables, including the transverse momentum and pseudo-rapidity of three-p_T ordered photons (γ_1, γ_2, and γ_3), the differences in the azimuthal angle and pseudo-rapidity between pairs of photons, the distance between pairs of photons in the $\eta - \varphi$ plane, and the invariant mass of the tri-photon system ($m_{\gamma_1\gamma_2\gamma_3}$). These variables were used as input to the TMVA package to perform multivariate analyses via the

BDT algorithm. In the final step, a threshold for the clipping energy value was applied to each aQGC parameter in the invariant mass distributions of tri-photon systems. Constraints on dimension-8 anomalous quartic gauge couplings, namely f_{T8}/Λ^4 and f_{T9}/Λ^4, are presented with and without a systematic uncertainty ($\delta \rightarrow$ 10%) at 3σ, 5σ, and 95%C.L. The analysis was carried out at FCC-hh with an integrated luminosity of 30 ab^{-1} and a center-of-mass energy of 100 TeV. Additionally, the analysis was performed at HL-LHC with an integrated luminosity of 3 ab^{-1} and a center-of-mass energy of 14 TeV. The constraints obtained at the 95% C.L. for the f_{T9}/Λ^4 and f_{T9}/Λ^4 couplings, using the clipping technique without accounting for systematic uncertainties, exhibit a strength that surpasses the most recent ATLAS limits by three orders of magnitude at FCC-hh collider. Even when a 10% systematic error was taken into account, the findings at 5σ and the 95% confidence level remained superior by two orders of magnitude compared to those recently communicated by current experimental limits at ATLAS. This underscored the robustness and substantial improvement over existing constraints.

5. REFERENCES

Vancouver citation system was used in this thesis.

1. Englert F, Brout R. Broken symmetry and the mass of gauge vector mesons. Physical Review Letters [Internet]. 1964 Aug 31 [cited 2023 Oct 21];13(9):321–3. Available from: https://journals.aps.org/prl/abstract/10.1103/PhysRevLett.13.321

2. Higgs PW. Broken symmetries and the masses of gauge bosons. Physical Review Letters [Internet]. 1964 Oct 19 [cited 2023 Oct 21];13(16):508–9. Available from: https://journals.aps.org/prl/abstract/10.1103/PhysRevLett.13.508

3. S. L. Glashow, Partial-Symmetries of Weak Interactions, Nuclear Physics 22 (1961) no. 4, 579 – 588.

4. A. Salam, Elementary Particle Theory. Almqvist and Wiksell, Stockholm, 1968.

5. S. Weinberg, A Model of Leptons, Phys. Rev. Lett. 19 (1967) 1264–1266.

6. J. Beringer et al., (Particle Data Group), Review of Particle Physics, Phys. Rev. D 86 (July, 2012).

7. D. Griffiths, Introduction to Elementary Particles, John Wiley & Son, 1987. check

8. Feynman RP. QED: The Strange Theory of Light and Matter. Princeton University Press; 1985.

9. Einstein A. The Field Equations of Gravitation. Sitzungsberichte der Königlich Preussischen Akademie der Wissenschaften. 1915;844–847.

10. Griffiths DJ. Introduction to Elementary Particles. Wiley; 2008.

11. F. Zwicky, "Die Rotverschiebung von extragalaktischen Nebeln," Helvetica Physica Acta, 1933.

12. A.G. Riess et al., "Observational Evidence from Supernovae for an Accelerating Universe and a Cosmological Constant," The Astronomical Journal, 1998. DOI: 10.1086/300499

13. J.C. Pati, A. Salam, "Lepton Number as the Fourth Color," Physical Review D, 1974. DOI: 10.1103/PhysRevD.10.275

14. M. Drees, R. Godbole, P. Roy, "Theory and Phenomenology of Sparticles: An Account of Four-Dimensional N=1 Supersymmetry in High-Energy Physics," World Scientific Publishing, 2004. DOI: 10.1142/5378

15. Greene B. The Elegant Universe: Superstrings, Hidden Dimensions, and the Quest for the Ultimate Theory. New York: W.W. Norton & Company; 1999.

16. Wolfenstein L. Neutrino Oscillations in Matter. Phys Rev D. 1978;17(9):2369-2374. doi:10.1103/PhysRevD.17.2369.

17. Mikheyev SP, Smirnov AY. Resonance Amplification of Oscillations in Matter and Spectroscopy of Solar Neutrinos. Sov J Nucl Phys. 1985;42:913.

18. Peccei RD, Quinn HR. CP Conservation in the Presence of Pseudoparticles. Phys Rev Lett. 1977;38:1440. DOI: 10.1103/PhysRevLett.38.1440.

19. Sikivie P. Experimental Tests of the 'Invisible' Axion. Phys Rev Lett. 1983;51:1415. DOI: 10.1103/PhysRevLett.51.1415.

20. M. Drees, R. Godbole, P. Roy, "Theory and Phenomenology of Sparticles: An Account of Four-Dimensional N=1 Supersymmetry in High-Energy Physics," World Scientific Publishing, 2004. DOI: 10.1142/5378

21. C. Degrande et al., "Effective field theory: A modern approach to anomalous couplings", Annals Phys. 335 (2013) 21, doi:10.1016/j.aop.2013.04.016, arXiv:1205.4231. check

22. O.J.P. Eboli, M.C. Gonzalez-Garcia, J.K. Mizukoshi, Phys. Rev. D 74 (2006) 073005, arXiv:hep-ph/0606118 [hep-ph].

23. C. Degrande, O. Eboli, B. Feigl, B. Jäger, W. Kilian, O. Mattelaer, M. Rauch, J. Reuter, M. Sekulla, D. Wackeroth, arXiv:1309.7890 [hep-ph].

24. G. Perez, M. Sekulla, D. Zeppenfeld, Eur. Phys. J. C 78 (9) (2018) 759, arXiv:1807.02707 [hep-ph].

25. E.d. Almeida, O.J.P. Éboli, M.C. Gonzalez–Garcia, Phys. Rev. D 101 (11) (2020) 113003, arXiv:2004.05174 [hep-ph].

26. ATLAS Collaboration, arXiv:2208.12741 [hep-ex].

27. K. Arnold, M. Bahr, G. Bozzi, F. Campanario, C. Englert, T. Figy, N. Greiner, C. Hackstein, V. Hankele, B. Jager, et al., Comput. Phys. Commun. 180 (2009) 1661–1670, arXiv:0811.4559 [hep-ph].

28. A. Tumasyan, et al., CMS, J. High Energy Phys. 10 (2021) 174, arXiv:2105.12780 [hep-ex].

29. A.M. Sirunyan, et al., CMS, Phys. Lett. B 812 (2021) 135992, arXiv:2008.07013 [hep-ex].

30. A. Tumasyan, et al., CMS, Phys. Rev. D 104 (2021) 072001, arXiv:2106.11082 [hep-ex].

31. A. Horvath, a schematical overview of LHC for Wikipedia, Nov. 2012. http://commons.wikimedia.org/wiki/File:LHC.svg.

32. LHC/HL-LHC Plan [Internet]. [cited 2023 Oct 3]. Available from: https://hilumilhc.web.cern.ch/sites/default/files/HL-LHC_Janvier2022.pdf

33. A. Abada et al., Fcc-hh: The hadron collider, The European Physical Journal Special Topics 228 (4) (2019) 755–1107. doi:10.1140/epjst/e2019-900087-0. URL https://doi.org/10.1140/epjst/e2019-900087-0

34. Monte Carlo Methods in Physics. Available from: https://www.cambridge.org/core/books/monte-carlo-methods-in-physics/2B1AEEEAB559CDAC9144C3525E05E695

35. MadGraph. Available from: https://madgraph.phys.ucl.ac.be/

36. FeynRules. Available from: https://feynrules.irmp.ucl.ac.be/

37. Pythia. Available from: http://home.thep.lu.se/~torbjorn/Pythia.html

38. Delphes. Available from: https://github.com/delphes/delphes

39. A. Alloul, N.D. Christensen, C. Degrande, C. Duhr, B. Fuks, Comput. Phys. Commun. 185 (2014) 2250, arXiv:1310.1921 [hep-ph].

40. C. Degrande, C. Duhr, B. Fuks, D. Grellscheid, O. Mattelaer, T. Reiter, Comput. Phys. Commun. 183 (2012) 1201–1214, arXiv:1108.2040 [hep-ph].

41. J. Alwall, et al., J. High Energy Phys. 1407 (2014) 079, arXiv:1405.0301 [hep-ph].

42. R.D. Ball, et al., Nucl. Phys. B 867 (2013) 244, arXiv:1207.1303 [hep-ph].

43. T. Sjöstrand, et al., Comput. Phys. Commun. 191 (2015) 159, arXiv:1410.3012 [hep-ph].

44. J. de Favereau, et al., DELPHES 3 Collaboration, J. High Energy Phys. 1402 (2014) 057, arXiv:1307.6346 [hep-ex].

45. M. Cacciari, G.P. Salam, G. Soyez, Eur. Phys. J. C 72 (2012) 1896, arXiv:1111.6097 [hep-ph].

46. M. Cacciari, G.P. Salam, G. Soyez, J. High Energy Phys. 0804 (2008) 063, arXiv:0802.1189 [hep-ph].

47. B.P. Roe, H.J. Yang, J. Zhu, Y. Liu, I. Stancu, G. McGregor, Nucl. Instrum. Methods A 543 (2–3) (2005) 577–584, arXiv:physics/0408124 [physics].

48. G. Carleo, I. Cirac, K. Cranmer, L. Daudet, M. Schuld, N. Tishby, L. Vogt-Maranto, L. Zdeborová, Rev. Mod. Phys. 91 (4) (2019) 045002, arXiv:1903.10563 [physics.comp-ph].

49. A. Hocker, et al., arXiv:physics/0703039 [physics.data-an].

50. Freund, Y., & Schapire, R. E. (1997). A Decision-Theoretic Generalization of On-Line Learning and an Application to Boosting. Journal of Computer and System Sciences, 55(1), 119–139. doi:10.1006/jcss.1997.1504

51. J.Therhaag, TMVA Core Developer Team, AIP Conf. Proc. 1504 (2009) 1013.

52. A. Hocker, et al., Schematic view of decision tree [Internet]. [cited 2023 Oct 3]. Available from: https://cds.cern.ch/record/1019880/files/BDTsketch.png

53. A. Senol, H. Denizli, C. Helveci Nucl. Phys. B 998, 116387 (2024) [arXiv:2303.14805 [hep-ph]].

54. A.M. Sirunyan, et al., CMS, Phys. Lett. B 809 (2020) 135710, arXiv:2005.01173 [hep-ex]. done

55. G. Cowan, K. Cranmer, E. Gross and O. Vitells, Eur. Phys. J. C 71, 1554 (2011) [erratum: Eur. Phys. J. C 73, 2501 (2013)] [arXiv:1007.1727 [physics.data-an]].